Low-mass bursty galaxies in JADES efficiently produce ionizing photons and could represent the main drivers of reionization

C. Simmonds [1,2]★ S. Tacchella [1,2] K. Hainline,[3] B. D. Johnson,[4] W. McClymont [1,2] B. Robertson,[5] A. Saxena [6,7] F. Sun,[3] C. Witten [1,8] W. M. Baker [1,2] R. Bhatawdekar,[9] K. Boyett,[10,11] A. J. Bunker,[6] S. Charlot,[12] E. Curtis-Lake,[13] E. Egami,[3] D. J. Eisenstein,[4] R. Hausen,[14] R. Maiolino,[1,2,7] M. V. Maseda,[15] J. Scholtz,[1,2] C. C. Williams,[16] C. Willott[17] and J. Witstok[1,2]

[1]*The Kavli Institute for Cosmology (KICC), University of Cambridge, Madingley Road, Cambridge CB3 0HA, UK*
[2]*Cavendish Laboratory, University of Cambridge, 19 JJ Thomson Avenue, Cambridge CB3 0HE, UK*
[3]*Steward Observatory, University of Arizona, 933 N. Cherry Avenue, Tucson, AZ 85721, USA*
[4]*Center for Astrophysics | Harvard & Smithsonian, 60 Garden St., Cambridge, MA 02138 USA*
[5]*Department of Astronomy and Astrophysics University of California, Santa Cruz, 1156 High Street, Santa Cruz CA 96054, USA*
[6]*Department of Physics, University of Oxford, Denys Wilkinson Building, Keble Road, Oxford OX1 3RH, UK*
[7]*Department of Physics and Astronomy, University College London, Gower Street, London WC1E 6BT, UK*
[8]*Institute of Astronomy, University of Cambridge, Madingley Road, Cambridge CB3 0HA, UK*
[9]*European Space Agency (ESA), European Space Astronomy Centre (ESAC), Camino Bajo del Castillo s/n, E-28692 Villanueva de la Cañada, Madrid, Spain*
[10]*School of Physics, University of Melbourne, Parkville 3010, VIC, Australia*
[11]*ARC Centre of Excellence for All Sky Astrophysics in 3 Dimensions (ASTRO 3D), Canberra 2611, Australia*
[12]*Institut d'Astrophysique de Paris, Sorbonne Université, CNRS, UMR 7095, 98 bis bd Arago, F-75014 Paris, France*
[13]*Department of Physics, Astronomy and Mathematics, Centre for Astrophysics Research, University of Hertfordshire, Hatfield AL10 9AB, UK*
[14]*Department of Physics and Astronomy, The Johns Hopkins University, 3400 N. Charles St., Baltimore, MD 21218, USA*
[15]*Department of Astronomy, University of Wisconsin-Madison, 475 N. Charter St., Madison, WI 53706, USA*
[16]*NSF's National Optical-Infrared Astronomy Research Laboratory, 950 North Cherry Avenue, Tucson, AZ 85719, USA*
[17]*NRC Herzberg, 5071 West Saanich Rd, Victoria, BC V9E 2E7, Canada*

ABSTRACT

We use deep imaging from the *JWST* Advanced Deep Extragalactic Survey (JADES) to study the evolution of the ionizing photon production efficiency, ξ_{ion}. We estimate ξ_{ion} for a sample of 677 galaxies at $z \sim 4$–9 using NIRCam (Near-Infrared Camera) photometry. Specifically, combinations of the medium and wide bands $F335M$–$F356W$ and $F410M$–$F444W$ to constrain emission lines that trace ξ_{ion}: Hα and [O III]. Additionally, we use the spectral energy distribution fitting code PROSPECTOR to fit all available photometry and infer galaxy properties. The flux measurements obtained via photometry are consistent with FRESCO (First Reionisation Epoch Spectroscopic Complete Survey) and NIRSpec-derived fluxes. Moreover, the emission-line-inferred measurements are consistent with the PROSPECTOR estimates. We also confirm the observed ξ_{ion} trend with redshift and M_{UV}, and find: $\log \xi_{ion}(z, M_{UV}) = (0.05 \pm 0.02)z + (0.11 \pm 0.02)M_{UV} + (27.33 \pm 0.37)$. We use PROSPECTOR to investigate correlations of ξ_{ion} with other galaxy properties. We see a clear correlation between ξ_{ion} and burstiness in the star formation history of galaxies, given by the ratio of recent to older star formation, where burstiness is more prevalent at lower stellar masses. We also convolve our ξ_{ion} relations with luminosity functions from the literature, and constant escape fractions of 10 per cent and 20 per cent, to place constraints on the cosmic ionizing photon budget. By combining our results, we find that if our sample is representative of the faint low-mass galaxy population, galaxies with bursty star formation are efficient enough in producing ionizing photons and could be responsible for the reionization of the Universe.

Key words: galaxies: evolution – galaxies: general – galaxies: high-redshift – dark ages, reionization, first stars.

1 INTRODUCTION

The Epoch of Reionization (EoR) describes one of the Universe's major phase changes, during which the intergalactic medium (IGM) became transparent to Lyman Continuum (LyC; $E \geq 13.6$ eV)

radiation. Observations place the end of this epoch at $z \sim 6$ (Becker et al. 2001; Fan et al. 2006; Yang et al. 2020), with some studies favouring a later reionization closer to $z \sim 5$ (Keating et al. 2020; Bosman et al. 2022). It is widely believed that young massive stars in galaxies are the main drivers of this transition, due to their copious production of LyC photons that escape the interstellar medium (ISM), and eventually ionize the IGM (Hassan et al. 2018; Rosdahl et al. 2018; Trebitsch, Volonteri & Dubois 2020). However, there is a

★ E-mail: cs2210@cam.ac.uk

debate whether faint low-mass galaxies, bright massive galaxies, or a combination of them, dominate the photon budget of reionization (Finkelstein et al. 2019; Naidu et al. 2020; Robertson 2022; Yeh et al. 2023). In particular, the mass of galaxies has been seen to correlate with both the production efficiency and escape of ionizing photons (Paardekooper, Khochfar & Dalla Vecchia 2015), both key factors to understand the EoR. Moreover, the contribution of active galactic nuclei (AGNs) to this budget might be more important than previously believed (AGN + host galaxy > 10 per cent; Maiolino et al. 2023). For galaxies to be the main sources of reionization, adopting canonical values of ionizing photon production efficiencies, relatively high average escape fractions are necessary (f_{esc} = 10 per cent–20 per cent, Ouchi et al. 2009; Robertson et al. 2013, 2015; Finkelstein et al. 2019; Naidu et al. 2020). High f_{esc} values have been observed in some galaxies (e.g. Borthakur et al. 2014; Bian et al. 2017; Vanzella et al. 2018; Izotov et al. 2021), but usually not in large samples (Leitet et al. 2013; Leitherer et al. 2016; Steidel et al. 2018; Flury et al. 2022). Another important quantity to measure is the ionizing photon production efficiency (ξ_{ion}), which is a measure of the production rate of ionizing photons over the non-ionizing ultraviolet (UV) luminosity density. Promisingly, by gaining observational access to the early Universe (up to $z \sim 9$), studies have found that as we go to higher redshifts, ξ_{ion} increases (e.g. Bouwens et al. 2016; Faisst et al. 2019; Endsley et al. 2021; Stefanon et al. 2022; Atek et al. 2023; Simmonds et al. 2023; Tang et al. 2023). An increase of ξ_{ion} implies that lower f_{esc} values are required in galaxies, in order for them to be responsible for the reionization of the Universe.

Current constraints place the mean redshift of reionization somewhere between $z = 7.8$–8.8 (Planck Collaboration XLVII 2016). Since the launch and deployment of the *JWST* (Gardner et al. 2023), we have an unprecedented view of the Universe deep into the EoR. Moreover, by using deep photometry taken with the Near-Infrared Camera (NIRCam; Rieke et al. 2023b), we can gain insight into the rest-frame optical properties of large and statistically significant samples of galaxies at this epoch. In particular, there are three important ingredients that contribute to our overall understanding of the ionizing photon budget of the Universe: (1) a prescription for the f_{esc} of the population, (2) an appropriate luminosity density function, ρ_{UV}, describing how many objects per unit volume of a certain UV luminosity exist as a function of redshift (e.g. Bouwens et al. 2021), and (3) ξ_{ion}. Until recently, it was common practice to set (1) and (3) as constants (e.g. Boyett et al. 2022). However, the launch of *JWST* has given us unprecedented access to the rest-frame optical regime at high redshift, providing enough additional constraints on the stellar population to better infer ξ_{ion} across the population. Therefore, studies shedding light on how f_{esc} and/or ξ_{ion} evolve with galaxy properties, especially at high redshift, are of utmost relevance to the field.

In Simmonds et al. (2023), *JWST* Extragalactic Medium Band Survey (JEMS; Williams et al. 2023) photometry was used to estimate ξ_{ion} for a sample of 30 Lyman-α emitters (LAEs) at $z \sim 6$. In this work, we use deep NIRCam imaging (Rieke et al. 2023a) to create a sample of 677 galaxies at $z \sim 4$–9, with photometric redshifts provided by the template-fitting code EAZY (Brammer, van Dokkum & Coppi 2008). We use two filter pair combinations: *F335M*–*F356W* and *F410M*–*F444W*, to estimate Hα and/or [O III] emission-line fluxes, which can be used to infer ξ_{ion}. To test the reliability of our derived fluxes, we compare (when available) our measurements to those obtained by First Reionisation Epoch Spectroscopic Complete Survey (FRESCO, Oesch et al. 2023, PI: Oesch) *grism* spectra. In addition, we compare our fluxes and ionizing photon production efficiencies to NIRSpec measurements (Saxena

et al. 2023). Simultaneously, we use the spectral energy distribution (SED) fitting code PROSPECTOR (Johnson et al. 2019, 2021) to infer galaxy properties such as star formation rates (SFRs) and histories (SFHs), both closely related to the production of ionizing photons through star formation. Finally, we investigate how our findings affect the cosmic ionizing photon budget, and make conclusions about which kind of galaxies could be the main sources responsible for the reionization of the Universe.

The structure of this paper is the following. In Section 2, we present the data used in this work, along with the sample selection criteria. In Section 3, we explain the two observational methods used to estimate ξ_{ion} (through Hα and [O III]$_{\lambda 5007}$), and how the respective fluxes were measured from photometry. In Section 4, we present our PROSPECTOR fitting method. Our ξ_{ion} constraints are given in Section 5, followed by a discussion in Section 6, and brief conclusions in Section 7.

Throughout this work we assume $\Omega_0 = 0.315$ and $H_0 = 67.4$ km s^{-1} Mpc^{-1}, following Planck Collaboration VI (2020).

2 DATA AND SELECTION CRITERIA

In this section, we describe the data and selection criteria applied to build a sample for which we can infer ξ_{ion} through emission-line fluxes, specifically Hα and [O III]$_{\lambda 5007}$. We caution the reader that by making this choice we are introducing a bias towards galaxies with strong emission lines, which will be discussed later.

2.1 Data

We make use of the NIRCam Deep imaging (Rieke et al. 2023a) released by the *JWST* Advanced Deep Extragalactic Survey (JADES; Eisenstein et al. 2023). This data cover an area of ~ 25 arcmin^2 overlapping with the Hubble Ultra Deep Field (Beckwith et al. 2006), and portions of the Great Origins Deeps Survey South (Giavalisco et al. 2004). The images were taken by a combination of nine medium- and wide-band infrared filters: *F090W*, *F115W*, *F150W*, *F200W*, *F277W*, *F335M*, *F356W*, *F410M*, and *F444W*. When in an overlapping region, some galaxies also have JEMS photometry, adding five more medium filters: *F182M*, *F210M*, *F430M*, *F460M*, and *F480M*. This exquisite data set is ideal to estimate photometric redshifts (photo-z) with great accuracy. In this work, we use photo-z inferred by the template-fitting code EAZY, as described in Hainline et al. (2023) and Rieke et al. (2023a).[1]

Regarding the photometric catalogue, the source detection and photometry leverage both the JEMS NIRCam medium band and JADES NIRCam broad- and medium-band imaging. Detection is performed using the PHOTUTILS (Bradley et al. 2022) software package, identifying sources with contiguous regions of the Signal-to-Noise Ratio (SNR) mosaic with signal $> 3\sigma$ and five or more contiguous pixels. We also use PHOTUTILS to perform circular aperture photometry with filter-dependent aperture corrections based on empirical point spread functions measured from stars in the mosaic. The details of the catalogue generation and photometry will be presented in Robertson et al. (in preparation). In this work, we adopt a circular aperture of diameter 0.3 arcsec throughout, and impose a floor error of 5 per cent in each band.

Finally, when available, we compare our photometry-derived emission-line fluxes to those obtained through an independent reduction of the spectra taken with the FRESCO program (Oesch

---

[1]For a visual comparison between the inferred photometric and spectroscopic redshifts, we refer the reader to fig. 13 of Rieke et al. (2023a).
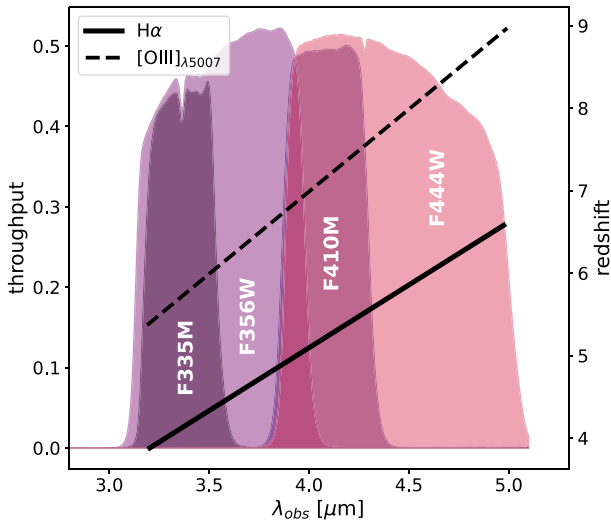
Figure 1. Medium- and wide-band NIRCam filters used to estimate Hα and/or [O III] emission-line fluxes in this work. From left to right: *F335M*, *F356W*, *F410M*, and *F444W*. The left *y*-axis indicates their throughput. The black lines show the observed wavelength of Hα (filled) and [O III]$_{\lambda5007}$ (dashed) with redshift (right axis). Depending on the redshift, the emission lines can be estimated by combining the medium- and wide-band filter pairs: *F335M*– *F356W* and/or *F410M*– *F444W*.

et al. 2023), which will be presented in Sun et al. (in preparation), and to NIRSpec measurements provided in Saxena et al. (2023).

2.2 Sample selection criteria

The focus of this work is to constrain ξ_{ion} for a large sample of emission-line galaxies, thought to have had a significant role in reionization (e.g. Rinaldi et al. 2023a, b). As is discussed in Section 3, this requires Hα and/or [O III]$_{\lambda5007}$ in emission. The combination of broad and medium photometric bands is powerful to estimate emission lines when spectra are not available (e.g. Bunker et al. 1995; Stark et al. 2013; Faisst et al. 2016). Therefore, we select galaxies where the desired emission lines fall on one (or more) of the following filters: *F335M*, *F356W*, *F410M* or *F444W*. Fig. 1 shows the throughput and wavelengths of these filters, as well as the redshift evolution of the observed wavelength of Hα and [O III]$_{\lambda5007}$. As shown in the right vertical axis, this constrains the sample to $z = 3.9$–9.0. We note that the medium bands from the JEMS survey cover a smaller region in the sky, therefore, we use them (when available) to feed our SED-fitting routine, but not for estimating emission-line fluxes.

We apply this redshift cut to galaxies based on their photo-*z*. Furthermore, in order to be able to detect emission lines, we impose a conservative minimum flux difference between medium and wide bands to ensure a 5σ line detection, as follows:

(i) $|F335M - F356W| \geq 10$ nJy,
(ii) $|F410M - F444W| \geq 10$ nJy,

where the excess in flux in a given band (depending on redshift) is assumed to be dominated by either Hα or [O III] (i.e. neglecting [N II], Hβ and [S II] contamination). A visual inspection was then performed on all the SEDs that satisfied this condition.

Once the sample has been constructed, we compare our flux excesses to a grid of simple CLOUDY (Ferland et al. 2017) photoionization models, using stellar populations from the Binary Population
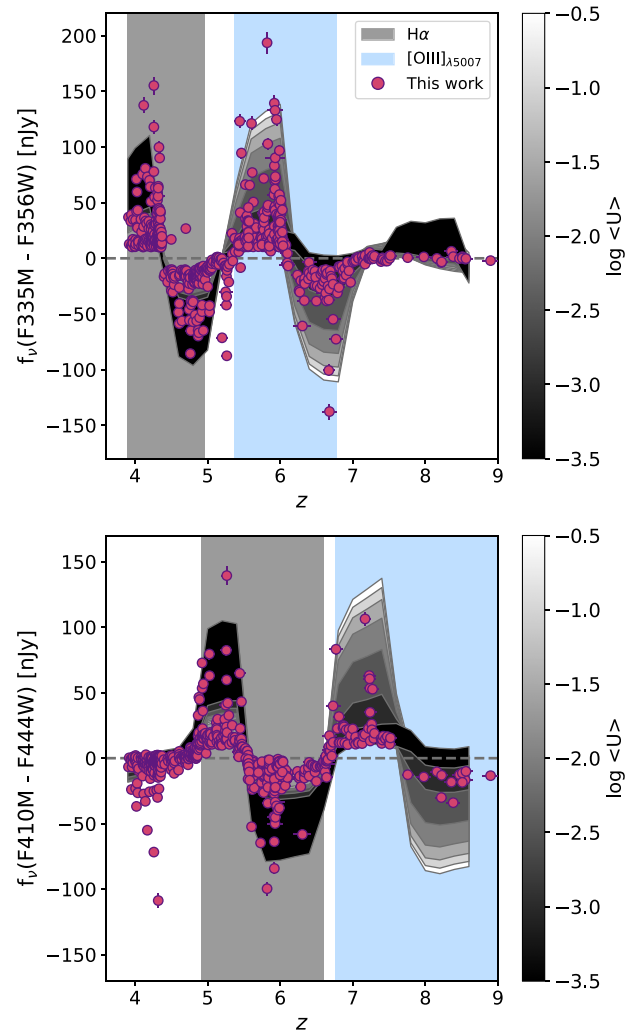

Figure 2. Expected shape for each filter pair flux differences, along with the corresponding emission lines, shown as vertical grey (Hα) and light blue ([O III]$_{[\lambda5007]}$) bands. The purple circles represent the sample analysed in this work, they overall follow the idealized CLOUDY models, shown as shaded areas colour-coded by ionization parameter ($\log\langle U\rangle$). This agreement corroborates the reliability of the photo-*z* inferred using EAZY. Fluxes are in units of nJy. Top panel: $F335M - F356W$. Bottom panel: $F410M - F444W$.

and Spectral Synthesis version 2.2.1 (Eldridge et al. 2017) as intrinsic SEDs. The models were run to convergence assuming a constant SFH. The stellar and nebular parameters were varied to cover a broad range of metallicities ($Z = 0.001, 0.006, 0.014$, and 0.030; in this convention $Z_\odot = 0.014$), ages ($3 \times 10^6, 5 \times 10^6, 10^7$, and 5×10^7 yr), ionization parameters ($\log\langle U\rangle = -3.5$ to -0.5 in steps of 0.5), and densities ($\log \rho/[\text{cm}^{-3}] = 0, 1, 2$, and 3). The net transmitted SEDs (that include nebular emission) were then redshifted between $z = 3.9$ and 9.0, in steps of 0.1, and photometry was simulated in the filters of interest (*F335M*, *F356W*, *F410M*, and *F444W*) using the code BAGPIPES (Carnall et al. 2018). Fig. 2 shows the results of this CLOUDY exercise, for visualization purposes the models are shown as shaded areas colour-coded by $\log\langle U\rangle$, and represent the shape expected in each filter pair, as a function of redshift. The regions where the respective emission lines dominate either filter pair are highlighted as vertical bands. As expected, there is a strong dependency of [O III]$_{\lambda5007}$ emission with $\log\langle U\rangle$. The final sample,

composed of 677 galaxies in the redshift range $z = 3.9$–8.9 is shown as purple circles.

3 USING PHOTOMETRY TO CONSTRAIN THE IONIZING PHOTON PRODUCTION EFFICIENCY OF GALAXIES

To estimate ξ_{ion} photometrically we use two methods, both of which rely on emission-line measurements, particularly Hα and [O III]$_{\lambda5007}$. We now briefly present them, along with a description of how they were applied in this work. We remind the reader that all errors in photometric points were floored to 5 per cent in these calculations.

3.1 Hα as proxy for ionizing radiation production

If we assume no ionizing photons escape from a galaxy ($f_{\mathrm{esc}} = 0$) and Case B recombination, the dust-corrected Hα luminosity is directly related to the amount of ionizing photons ($\dot{n}_{\mathrm{ion}}$) that are being emitted. Adopting a temperature of 10^4 K and an electron density of 100 cm^{-3}, these quantities are related by:

$$\dot{n}_{\mathrm{ion}} = 7.28 \times 10^{11} \, L(\mathrm{H}\alpha), \qquad (1)$$

as given in Osterbrock & Ferland (2006), where $\dot{n}_{\mathrm{ion}}$ is in units of photon s^{-1}, and L(Hα) in erg s^{-1}. This equation has a slight dependence on temperature and metallicity (Charlot & Longhetti 2001), but for the purpose of this work this has been ignored. We note that the Case B recombination assumption yields a conservative estimation of the amount of ionizing photons being produced, and non-zero escape fractions would lead to a boost in the derived $\dot{n}_{\mathrm{ion}}$ values. Additionally, instead of ionizing the surrounding gas or escaping, a significant amount of ionizing photons could be absorbed by dust ($\sim$30 per cent; Tacchella et al. 2023), resulting in a lack of nebular emission lines.

To estimate the ionizing photon production efficiency per UV luminosity assuming Case B recombination, $\xi_{\mathrm{ion},0}$ (the zero subscript indicates $f_{\mathrm{esc}} = 0$), we insert $\dot{n}_{\mathrm{ion}}$ into the following equation:

$$\xi_{\mathrm{ion},0} = \frac{\dot{n}_{\mathrm{ion}}}{L_{\mathrm{UV}}}, \qquad (2)$$

where L_{UV} is the observed monochromatic luminosity in units of erg s^{-1} Hz^{-1}, measured at the rest-frame wavelength of $\lambda = 1500$ Å.

3.1.1 Measurements from photometry

We define four redshift bins to estimate Hα fluxes, based the expected wavelength of Hα, as follows:

(i) $3.90 \leq z \leq 4.37$: $f(\mathrm{H}\alpha)$ falls in *F335M*,
(ii) $4.37 < z < 4.92$: $f(\mathrm{H}\alpha)$ falls in *F356W*, but outside *F335M,*
(iii) $4.92 \leq z \leq 5.61$: $f(\mathrm{H}\alpha)$ falls in *F410M*,
(iv) $5.61 < z \leq 6.59$: $f(\mathrm{H}\alpha)$ falls in *F444W*, but outside *F410M,*

where we assume the excess flux in the filter containing Hα is dominated by Hα emission, reasonable at high redshifts (e.g. Cameron et al. 2023). To obtain L_{UV}, we fit a straight line in logarithmic space using the `curve_fit` function in SCIPY (Virtanen et al. 2020), between rest frame 1250 and 2500 Å, in the form $f_\lambda \propto \lambda^\beta$, where β is the rest-frame UV continuum slope (β; Calzetti, Kinney & Storchi-Bergmann 1994). We use all the available photometry in this region for each redshift bin.

Fig. 3 shows a representative example SED of each Hα redshift bin. The identifier and redshift of each galaxy are given in the caption. The expected wavelengths of Hα and [O III]$_{\lambda5007}$ are shown as vertical

lines, it can be seen that Hα falls primarily in a different filter as redshift increases. The photometry of the four NIRCam filters of interest are highlighted with red edges. The β slope is given in the legend, and corresponds to the purple dashed line. Finally, the blue cross shows the observed wavelength and flux corresponding to rest-frame 1500 Å.

Once Hα fluxes have been calculated, they must be corrected for dust attenuation. This is not trivial for our sample since this parameter is not well understood at high redshifts (Gallerani et al. 2010; Ma et al. 2019), and we do not have measurements for Balmer line ratios. Moreover, the geometry and effect of dust attenuation in early galaxies is highly uncertain (Bowler et al. 2018, 2022). Nevertheless, it has been shown that a steep attenuation curve, such as seen in the Small Magellanic Cloud (SMC, Prevot et al. 1984; Gordon & Clayton 1998), is appropriate for young high-redshift galaxies (Shivaei et al. 2020). Thus, we apply an average SMC attenuation curve (Gordon et al. 2003) to our Hα and UV measurements, using β to infer the nebular continuum colour excess $E(B - V)$, given by $E(B - V) = (\beta + 2.616) \times \frac{1}{11.259}$ (Reddy et al. 2018,; adopting SMC attenuation).

We note that in redshift bins (ii) and (iv), Hα falls in the wide-band filter, and thus, more noise is introduced. In addition, they could be affected by [N II] and/or [S II] contamination. As discussed in Simmonds et al. (2023), this contamination is not expected to be significant at high redshift (see also Maiolino & Mannucci 2019; Onodera et al. 2020; Sugahara et al. 2022; Cameron et al. 2023).

3.2 [O III] equivalent widths as proxy for ionizing radiation production

The previous method has some limitations, such as the assumption of Case B recombination, and the high dependence on the attenuation curve adopted. Moreover, at $z \gtrsim 6$, Hα is redshifted to wavelengths challenging to observe. To circumvent these limitations, an alternative method that depends on [O III]$_{\lambda5007}$ instead was proposed in Chevallard et al. (2018), granting access to higher redshifts (up to $z \sim 9.5$). Strong [O III] emission is indicative of intense ionization conditions, such as those found at the early Universe. In brief, they use 10 local analogues ($z \sim 0$) to high-redshift galaxies and derive an empirical relation between ξ_{ion} and [O III]$_{\lambda5007}$ equivalent widths (EWs). Tang et al. (2019) conducted a similar project but with a larger sample and at higher redshift ($z \sim 2$). Since their sample is closer in parameter space to ours, we follow equation (4) of their work,

$$\log \xi_{\mathrm{ion}} = (0.73 \pm 0.08) \times \log(\mathrm{EW} \, [\mathrm{O\,III}]_{\lambda5007}) + (23.45 \pm 0.23), \qquad (3)$$

assuming an SMC attenuation law.

3.2.1 Measurements from photometry

As in the Hα case, we define four redshift bins to estimate [O III]$_{\lambda5007}$ fluxes, as follows:

(i) $5.37 \leq z \leq 6.15$: $f([\mathrm{O\,III}]_{\lambda5007})$ falls in *F335M*,
(ii) $6.15 < z < 6.77$: $f([\mathrm{O\,III}]_{\lambda5007})$ falls in *F356W*, but outside *F335M*,
(iii) $6.77 \leq z \leq 7.55$: $f([\mathrm{O\,III}]_{\lambda5007})$ falls in *F410M*,
(iv) $7.55 < z \leq 9.00$: $f([\mathrm{O\,III}]_{\lambda5007})$ falls in *F444W*, but outside *F410M*.
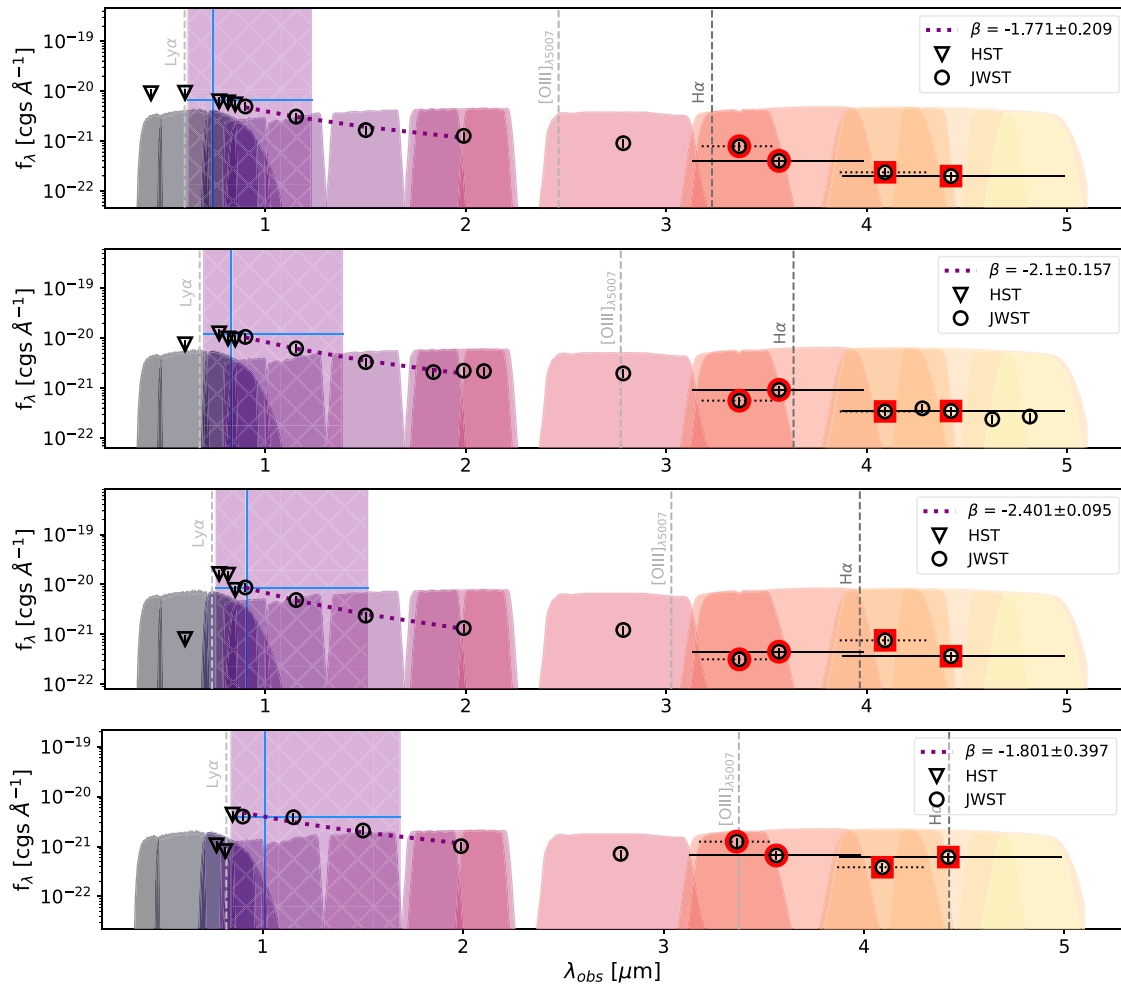
Figure 3. Representative example SEDs of each Hα redshift bin, with redshift increasing downward. From top to bottom: JADES-GS + 53.20925−27.75711 ($z =$ 3.92 ± 0.04), JADES-GS + 53.11398−27.80615 ($z = 4.54 ± 0.05$), JADES-GS + 53.15638−27.80966 ($z = 5.04 ± 0.08$), and JADES-GS + 53.15825−27.74091 ($z = 5.74 ± 0.06$). The coloured curves show the transmission of the filters used in this work. Specifically, the *HST*/ACS bands: *F435W*, *F606W*, *F775W*, *F814W*, and *F850LP*. Followed by the JADES NIRCam bands: *F090W*, *F115W*, *F150W*, *F200W*, *F277W*, *F335M*, *F356W*, *F410M*, and *F444W*. Finally (when available), JEMS medium-band photometry in the bands: *F182M*, *F210M*, *F430M*, *F460M*, and *F480M*. *HST* fluxes are shown as triangles, while the circles show *JWST* NIRCam photometry. The photometry of the filter pairs of interest are highlighted in red (circles for *F335M* − *F356W* and squares for *F410M* − *F444W*). The purple vertical hatched band marks the rest-frame 1250–2500 Å region. The β slope is given in the legend of each panel, and corresponds to the purple dotted line. Finally, the blue cross shows the observed wavelength and flux corresponding to rest-frame 1500 Å. For every redshift bin, the Hα line falls dominantly on either *F335M*, *F356W*, *F410M*, or *F444W*. The detection and flux measurement of [O III]$_{\lambda 5007}$ is performed in an analogous manner.

Our data allows us to estimate [O III]$_{\lambda\lambda 4959 + 5007}$ fluxes, therefore, to obtain [O III]$_{\lambda 5007}$, we adopt the standard ratio between the components of the [O III] doublet: [O III]$_{\lambda 5007} = 0.75 \times$ [O III]$_{\lambda\lambda 4959, 5007}$. Unless stated differently, all [O III] fluxes in this work hereafter represent [O III]$_{\lambda 5007}$. The EWs are then the division between the [O III] line fluxes and the local continuum. The latter was estimated following two prescriptions depending if the line falls on the medium or the wide band of each filter pair (*F335M* − *F356W* or *F410M* − *F444W*). If the line falls in the medium band, then the wide band also includes it, so the local continuum is measured from the corresponding wide band minus the line contribution. On the other hand, if the line falls in the wide band, then the corresponding medium band is assumed to represent the continuum. The differential dust attenuation between continuum and nebular emission is uncertain at high redshifts. Here, we assume a ratio of 1.3 between the reddening affecting emission lines and continuum,

appropriate at $z \sim 1$ (Pannella et al. 2015), but caution that this value can be closer to 2 for galaxies with low metallicities (Shivaei et al. 2020). Adopting the latter would systematically increase our [O III] EWs and consequently, our inferred ξ_{ion} measurements. We note that [O III] might suffer from Hβ contamination, below we investigate the importance of this contamination by comparing our fluxes to those measured in FRESCO *grism* spectra.

3.3 Flux comparisons to FRESCO *grism* spectra

To investigate the importance of contamination from other emission lines in our Hα and [O III] fluxes, as well as to test the simplistic approach to measuring the fluxes, we compare our measurements (when available) with those obtained through an independent reduction of FRESCO *grism* spectra. The detailed FRESCO grism line flux measurements and validation for a larger sample of $z =$
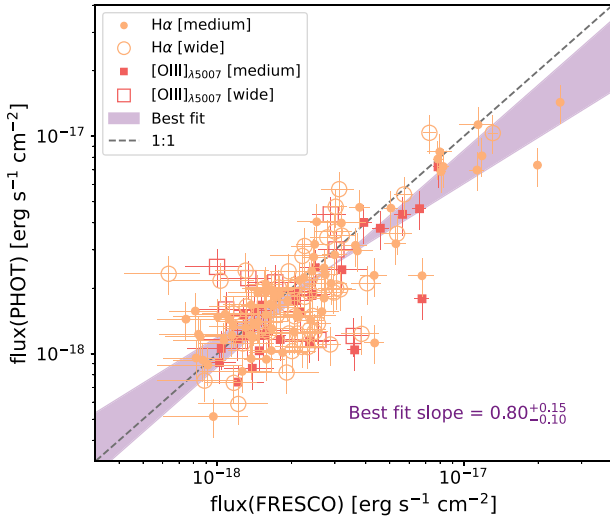
Figure 4. Comparison of fluxes obtained via photometry with those obtained through FRESCO *grism* spectra (when available). There are 122 overlapping cases with Hα fluxes (orange circles), and 36 with [O III]$_{λ5007}$ fluxes (red squares). The filled and open symbols indicate if the emission line falls predominantly in a medium (*F335M* or *F410M*) or wide (*F356W* or *F444W*) band. The shaded area shows the best fit to the data and its corresponding errors, with a best-fitting slope of $0.80^{+0.15}_{-0.10}$. We find the values obtained by photometry in this work are in significant agreement with those measured with *grism* spectra, although somewhat underestimated at the brightest end, suggesting there is minimal contamination from other emission lines ([N II], [S II], and Hβ). The fluxes that fall in wide bands contain more continuum and noise, resulting in a larger scatter. We note the background subtraction in *grism* spectra can lead to an underestimation of emission-line fluxes. In a similar manner, our photometrically derived fluxes have a fixed aperture of diameter 0.3 arcsec, and might not capture the total flux of a source.

5–9 galaxies will be presented in a forthcoming paper (Sun et al. in preparation). We find 122 (36) overlapping galaxies with Hα ([O III]) flux measurements. Fig. 4 shows the results for both Hα (circles) and [O III] (squares). The filled and open symbols in each case denote if the emission line falls in a medium or wide band, respectively. Our line flux estimations broadly trace the FRESCO measurements, confirming that our approach, while simplistic, is overall acceptable. Moreover, it indicates that if other lines are contaminating our flux estimations ([N II] or [S II] in the case of Hα, Hβ in the case of [O III]), then the contribution is not significant on average. We draw attention to the limitations of estimating emission-line fluxes using these two methods: *grism* spectra can potentially be affected by background subtraction, while aperture photometry can neglect some flux in extended sources. Both cases would lead to an underestimation in the measurement of emission-line fluxes.

4 SED FITTING WITH PROSPECTOR

We use the galaxy SED fitting code PROSPECTOR (Johnson et al. 2019, 2021) to study our sample, and compare to our ξ_{ion} estimations. This code uses photometry and/or spectroscopy as an input in order to infer stellar population parameters, from UV to IR wavelengths. In this work, we use photometry from the *Hubble Space Telescope* (*HST*) Advanced Camera for Surveys (ACS) bands: *F435W* (λ_{eff} = 0.432 μm), *F606W* (λ_{eff} = 0.578 μm), *F775W* (λ_{eff} = 0.762 μm), *F814W* (λ_{eff} = 0.803 μm), and *F850LP* (λ_{eff} = 0.912 μm). In addition, we use the JADES NIRCam photometry from: *F090W* (λ_{eff} =

0.898 μm), *F115W* (λ_{eff} = 1.143 μm), *F150W* (λ_{eff} = 1.487 μm), *F200W* (λ_{eff} = 1.968 μm), *F277W* (λ_{eff} = 2.786 μm), *F335M* (λ_{eff} = 3.365 μm), *F356W* (λ_{eff} = 3.563 μm), *F410M* (λ_{eff} = 4.092 μm), and *F444W* (λ_{eff} = 4.421 μm). Finally, when available, we include JEMS photometry: *F182M* (λ_{eff} = 1.829 μm), *F210M* (λ_{eff} = 2.091 μm), *F430M* (λ_{eff} = 4.287 μm), *F460M* (λ_{eff} = 4.627 μm), and *F480M* (λ_{eff} = 4.814 μm). The same circular aperture of diameter 0.30 arcsec is used to extract the *HST*, JADES, and JEMS convolved photometry. All photometry has been aperture corrected.

For the redshift, we adopt a normal distribution using the EAZY photo-z as a mean, with the sigma given by the photo-z errors. We vary the dust attenuation and stellar population properties following Tacchella et al. (2022a). In particular, we use a two-component dust model described in Conroy, Gunn & White (2009). This model accounts for the differential effect of dust on young stars (<10 Myr) and nebular emission lines, through a variable dust index. We adopt a Chabrier initial mass function (Chabrier 2003), with mass cut-offs of 0.1 and 100 M$_\odot$, respectively, allowing the stellar metallicity to explore a range between 0.01–1 Z$_\odot$, and include nebular emission. The continuum and emission properties of the SEDs are provided by the Flexible Stellar Population Synthesis (FSPS) code (Byler et al. 2017), based on CLOUDY models (v.13.03; Ferland et al. 2013). This earlier version of CLOUDY introduces an upper limit on the permitted ionization parameters ($\log\langle U\rangle_{max} = -1.0$). Due to the stochastic nature of the IGM absorption, we set a flexible IGM model based on a scaling of the Madau (1995) model, with the scaling left as a free parameter with a clipped normal prior ($\mu = 1.0$ and $\sigma = 0.03$, in a range [0.0, 2.0]). Last but not least, we use a non-parametric SFH (continuity SFH; Leja et al. 2019). This model describes the SFH as six different SFR bins, the ratios and amplitudes between them are in turn, controlled by the bursty-continuity prior (Tacchella et al. 2022b).

In this work, we use PROSPECTOR to calculate ξ_{ion} for our entire sample, as well as to infer galaxy properties. The latter can be found in Appendix A. PROSPECTOR has the ability to reconstruct the full SED of galaxies, therefore, ξ_{ion} is calculated from direct integration of the spectra, allowing to marginalize over most of the assumptions made for the most direct observational estimates from the emission-line excess presented in Section 3.

5 CONSTRAINTS ON ξ_{ION}

After confirming the overall consistency of our flux measurements, we estimate ξ_{ion} following the methods described in Section 3, and compare them to those inferred by PROSPECTOR. We provide an excerpt of the results in Table 1, and present them visually in Fig. 5. A comparison between the values inferred from emission lines and relevant values from literature can be found in Fig. 6. We find a good agreement between the ξ_{ion} obtained through Hα, [O III], and PROSPECTOR, this agreement is highlighted in Fig. 7. In addition, we include seven LAEs studied in Saxena et al. (2023) using NIRSpec spectra, for which ξ_{ion} was measured directly from Balmer recombination lines (Hα and Hβ). These seven LAEs overlap with our sample and our results are consistent with theirs (see Table 2). Moreover, our ξ_{ion} values agree with those found in literature. For example, Stefanon et al. (2022) compiled ξ_{ion} measurements up to $z \sim 8$ (using data points from Stark et al. 2015, 2017; Bouwens et al. 2016; Mármol-Queraltó et al. 2016; Nakajima et al. 2016; Matthee et al. 2017; Harikane et al. 2018; Shivaei et al. 2018; De Barros et al. 2019; Faisst et al. 2019; Lam et al. 2019; Tang et al. 2019; Emami et al. 2020; Nanayakkara et al. 2020; Endsley et al. 2021; Atek et al. 2022; Naidu et al. 2022). With this extensive compilation,

Table 1. Table excerpt showing a selection of galaxies in our sample. Depending on the redshift and the detection of emission lines, galaxies can have ξ_{ion} estimations from Hα, [O III]$_{\lambda 5007}$, or both.

Name	z	log $\xi_{ion, 0}$ (Hα) [Hz erg^{-1}]	log ξ_{ion} ([O III]) [Hz erg^{-1}]	log ξ_{ion} (PROSPECTOR) [Hz erg^{-1}]
JADES-GS + 53.11634−27.81272	3.9094 ± 0.0476	$25.26^{+0.30}_{-0.30}$	–	$25.48^{+0.03}_{-0.06}$
JADES-GS + 53.20925−27.75711	3.9196 ± 0.0379	$25.52^{+0.30}_{-0.30}$	–	$25.52^{+0.04}_{-0.04}$
JADES-GS + 53.12549−27.78044	3.9413 ± 0.0462	$25.17^{+0.30}_{-0.30}$	–	$25.35^{+0.05}_{-0.03}$
JADES-GS + 53.18436−27.80581	3.9496 ± 0.0402	$25.43^{+0.30}_{-0.30}$	–	$25.19^{+0.17}_{-0.14}$
JADES-GS + 53.16268−27.73611	3.9496 ± 0.0399	$25.31^{+0.30}_{-0.30}$	–	$25.37^{+0.06}_{-0.06}$
JADES-GS + 53.15123−27.79826	3.9595 ± 0.0446	$25.24^{+0.30}_{-0.30}$	–	$25.01^{+0.18}_{-0.15}$
JADES-GS + 53.15282−27.79549	3.9688 ± 0.0417	$25.43^{+0.30}_{-0.30}$	–	$25.71^{+0.03}_{-0.04}$
JADES-GS + 53.19804−27.76002	3.9696 ± 0.0421	$25.25^{+0.30}_{-0.30}$	–	$25.39^{+0.04}_{-0.05}$
JADES-GS + 53.13905−27.75893	3.9740 ± 0.0515	$25.39^{+0.30}_{-0.30}$	–	$25.65^{+0.03}_{-0.01}$
JADES-GS + 53.15186−27.75258	3.9992 ± 0.0561	$25.34^{+0.30}_{-0.30}$	–	$25.58^{+0.07}_{-0.04}$
JADES-GS + 53.12644−27.79200	5.3746 ± 0.0581	$25.47^{+0.30}_{-0.30}$	$25.55^{+0.32}_{-0.29}$	$25.77^{+0.07}_{-0.04}$
JADES-GS + 53.12775−27.78098	5.3751 ± 0.0650	$25.38^{+0.30}_{-0.30}$	$25.45^{+0.32}_{-0.29}$	$25.52^{+0.05}_{-0.04}$
JADES-GS + 53.16729−27.75273	5.3785 ± 0.0617	$25.28^{+0.30}_{-0.30}$	$25.21^{+0.31}_{-0.29}$	$25.45^{+0.05}_{-0.07}$
JADES-GS + 53.14381−27.80835	5.4189 ± 0.0763	$25.27^{+0.30}_{-0.30}$	$25.60^{+0.32}_{-0.29}$	$25.72^{+0.04}_{-0.05}$
JADES-GS + 53.10726−27.81102	5.4290 ± 0.0729	$25.90^{+0.30}_{-0.30}$	$25.61^{+0.32}_{-0.29}$	$25.88^{+0.08}_{-0.03}$
JADES-GS + 53.14676−27.79738	5.4294 ± 0.0578	$25.36^{+0.30}_{-0.30}$	$25.52^{+0.32}_{-0.29}$	$25.71^{+0.03}_{-0.05}$
JADES-GS + 53.12301−27.79661	5.4393 ± 0.0601	$25.57^{+0.30}_{-0.30}$	$25.50^{+0.32}_{-0.29}$	$25.80^{+0.02}_{-0.02}$
JADES-GS + 53.12247−27.79653	5.4418 ± 0.0666	$25.49^{+0.30}_{-0.30}$	$25.44^{+0.32}_{-0.29}$	$25.67^{+0.05}_{-0.05}$
JADES-GS + 53.16407−27.79972	5.4422 ± 0.0826	$25.40^{+0.30}_{-0.30}$	$25.45^{+0.32}_{-0.29}$	$25.05^{+0.11}_{-0.11}$
JADES-GS + 53.12874−27.79788	5.4430 ± 0.0572	$25.41^{+0.30}_{-0.30}$	$25.44^{+0.32}_{-0.29}$	$25.65^{+0.06}_{-0.05}$
JADES-GS + 53.19106−27.79732	7.2634 ± 0.0745	–	$25.44^{+0.32}_{-0.29}$	$25.57^{+0.11}_{-0.16}$
JADES-GS + 53.17976−27.77465	7.2717 ± 0.0805	–	$25.57^{+0.32}_{-0.29}$	$25.63^{+0.07}_{-0.03}$
JADES-GS + 53.16579−27.82179	7.2890 ± 0.0873	–	$25.63^{+0.32}_{-0.29}$	$25.73^{+0.15}_{-0.05}$
JADES-GS + 53.18334−27.79050	7.2994 ± 0.0665	–	$25.76^{+0.32}_{-0.28}$	$25.71^{+0.09}_{-0.05}$
JADES-GS + 53.13219−27.78578	7.3890 ± 0.0851	–	$25.74^{+0.32}_{-0.28}$	$25.73^{+0.18}_{-0.10}$
JADES-GS + 53.16638−27.81237	7.3992 ± 0.0762	–	$25.68^{+0.32}_{-0.29}$	$25.80^{+0.02}_{-0.08}$
JADES-GS + 53.18405−27.79783	7.4091 ± 0.0826	–	$25.60^{+0.32}_{-0.29}$	$25.71^{+0.06}_{-0.05}$
JADES-GS + 53.18536−27.77319	7.4095 ± 0.0590	–	$25.57^{+0.32}_{-0.29}$	$25.62^{+0.28}_{-0.15}$
JADES-GS + 53.18393−27.79999	7.4193 ± 0.0719	–	$25.45^{+0.32}_{-0.29}$	$25.62^{+0.06}_{-0.10}$
JADES-GS + 53.18301−27.78946	7.4494 ± 0.0672	–	$25.63^{+0.32}_{-0.29}$	$25.91^{+0.03}_{-0.17}$

Notes. Column 1: JADES identifier, composed of the coordinates of the centroid rounded to the fifth decimal place, in units of degrees. Column 2: photometric redshift from inferred using the template-fitting code EAZY. Columns 3–5: logarithm of the ionizing photon production efficiency estimations in units of Hz erg^{-1}. Columns 4 and 5 have values obtained through photometry using the Hα and [O III] methods, the uniformity in their errors arises from flooring the photometric uncertainties. Column 6 values where provided by PROSPECTOR.

they provided a best fit to the slope of ξ_{ion} as a function of redshift (given by dlog $\xi_{ion, 0}$/d$z = 0.09 \pm 0.01$), which is consistent within errors with this work (dlog ξ_{ion}/d$z = 0.07 \pm 0.02$). More recently, *JWST* has been used to estimate ξ_{ion} for individual galaxies up to $z \sim 8$ (see Ning et al. 2023; Prieto-Lyon et al. 2023; Simmonds et al. 2023; Rinaldi et al. 2023a), and this work is also consistent with those. In the bottom panel of Fig. 5, ξ_{ion} is shown as a function of redshift but colour-coded by M_{UV}. The horizontal dashed lines show the intercepts of the best-fitting relations between ξ_{ion} and M_{UV} per redshift bin, discussed in the next paragraph, for a constant M_{UV} of -18. Their increase demonstrates that for a fixed M_{UV}, ξ_{ion} evolves with redshift.

ξ_{ion} has been shown to vary due to the metallicity, age, and dust content of galaxies (Shivaei et al. 2018), as well as due to their UV luminosities (Duncan & Conselice 2015), where fainter galaxies are more efficient at producing ionizing radiation. This is clearly illustrated in fig. 3 from Maseda et al. (2020), which consists of a compilation of measurements from literature (specifically; Bouwens et al. 2016; Matthee et al. 2017; Harikane et al. 2018; Lam et al. 2019). We check for this relation in our data and find a similar trend, shown in Fig. 8. For clarity, the sample is separated into redshift bins. As expected, there are less galaxies in the higher redshift bins, however, we consistently find the fainter galaxies in our sample have increased ξ_{ion}. In addition, the higher redshift bins in our sample ($z > 7$) are populated by fainter galaxies than the other bins. This is potentially a result of our selection function, and will be discussed later. We note that an opposite trend is seen with $\dot{n}_{ion}$, namely, that $\dot{n}_{ion}$ decreases for fainter galaxies (see Appendix B). Given the observed trends of ξ_{ion} with redshift and M_{UV}, and the reliability of the PROSPECTOR-inferred ξ_{ion} (and M_{UV}) measurements for our sample, we perform a two-dimensional line fit combining these parameters and find:

$$\log \xi_{ion}(z, M_{UV}) = (0.05 \pm 0.02)z + (0.11 \pm 0.02)M_{UV}$$
$$+ (27.33 \pm 0.37), \qquad (4)$$

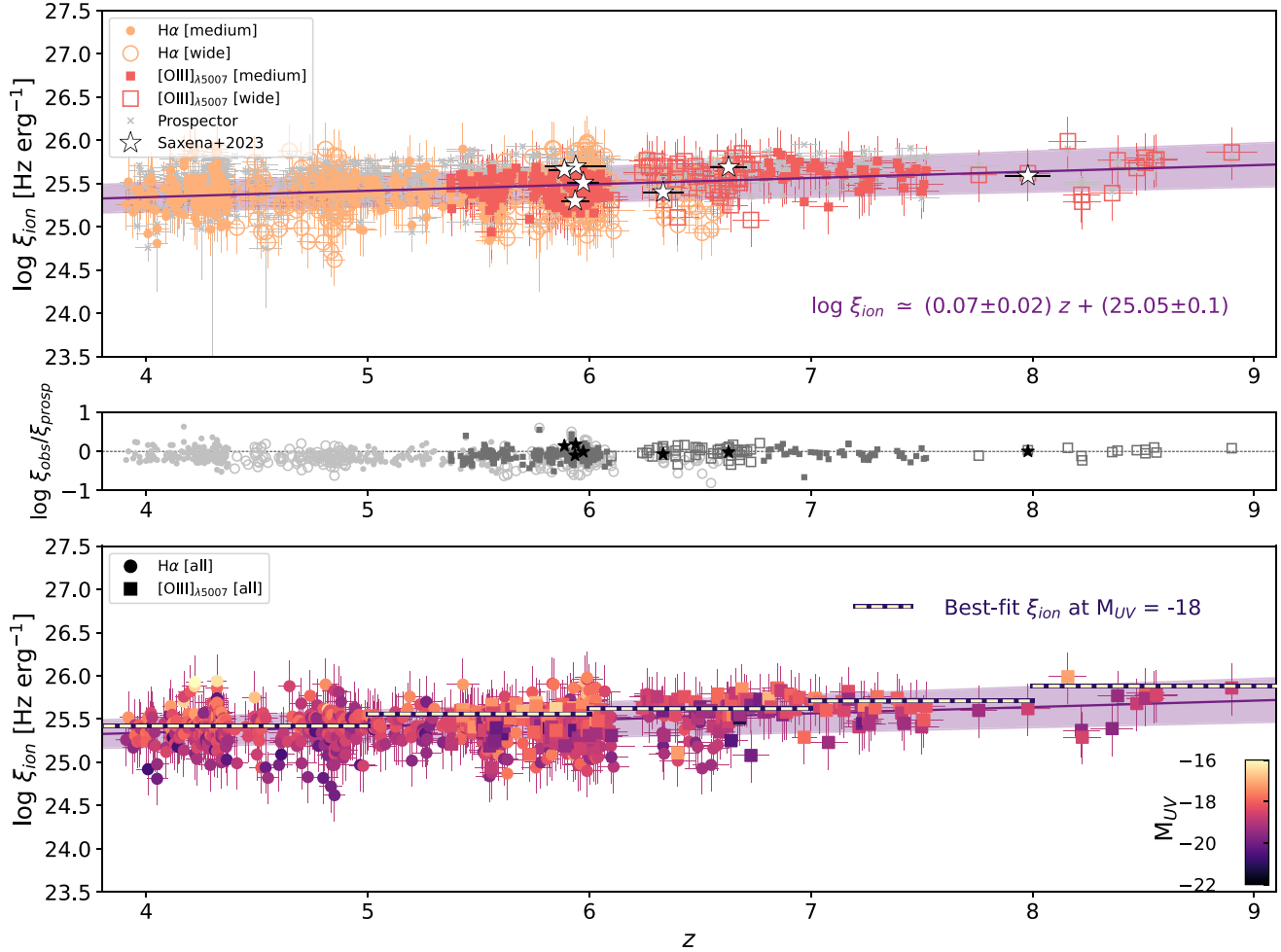**Figure 5.** ξ_{ion} values inferred through Hα and [O III]$_{\lambda5007}$ emission lines, as well as through through SED fitting. For comparison, we include NIRSpec measurements for seven galaxies from Saxena et al. (2023) that overlap with our sample (white stars), most of which were derived from Hα fluxes. We note that for the Hα and [O III]$_{\lambda5007}$ results, an SMC dust attenuation curve was assumed, and remind the reader that the Hα method in addition assumes an escape fraction of zero. Top panel: ξ_{ion} versus redshift for the entire sample (677 galaxies). The symbols and colours of the values estimated by photometry are the same as in Fig. 4. The PROSPECTOR estimations are shown in grey. The line represents the best fit to the photometrically inferred results. As expected, there is more scatter when the emission lines fall on wide bands (either *F356W* or *F444W*), due to more noise and continuum being introduced. Middle panel: residuals between the values inferred through photometrically estimated emission lines and via PROSPECTOR. The symbols are the same as in the upper panel, light grey corresponds to comparisons with the Hα method, while dark grey corresponds to comparisons with the [O III]$_{\lambda5007}$ method. We find a good agreement between all methods, and confirm an increased ξ_{ion} with redshift given by $\log \xi_{ion} = (0.07 \pm 0.02)z + 25.05 \pm 0.11$, consistent with literature (see Fig. 6). Bottom panel: same as top panel but only showing the photometrically estimated ξ_{ion} values, and colour-coded by M_{UV}. The dashed horizontal lines represent the intercepts of the best-fitting relations shown in Fig. 8 for a fixed M_{UV} of -18. It can be seen that at fixed M_{UV}, ξ_{ion} evolves with redshift.

where ξ_{ion} is in units of Hz erg^{-1}. This equation simultaneously describes the positive evolution of ξ_{ion} with z and M_{UV}, which is shown in Fig. 5.

Regarding the use of [O III] EWs to estimate ξ_{ion}, in Fig. 9 we present an update to a figure from Tang et al. (2019), showing how ξ_{ion} and [O III] EWs correlate. We plot their $z \sim 2$ results, along with the local ones from Chevallard et al. (2018), and the ones estimated for a sample of extreme emission-line galaxies (EELGs) at $z \sim 3$–6.7 in Boyett et al. (in preparation). We include our [O III] EWs obtained from photometry and the ξ_{ion} from PROSPECTOR. We remind the reader that the use of a fixed circular aperture in the photometry might result in an underestimation of fluxes when sources are extended. Additionally, differences in dust treatments affect the EW measurements, for example, adopting a higher ratio between nebular and continuum dust attenuation would increase the

measurements of this work. We attribute the differences between our sample and the EELGs from Boyett et al. (in preparation) to a combination of the fixed circular aperture choice and the adopted dust attenuation assumptions. Independent of these slight discrepancies, however, for every sample, ξ_{ion} increases with [O III] EWs. This connection between ξ_{ion} and [O III] EWs has also been seen in some simulations, for example, Seeyave et al. (2023) report a positive correlation between [O III] EWs and ξ_{ion} in the First Light And Reionisation Epoch Simulations (Lovell et al. 2021; Vijayan et al. 2021). Our results broadly follow the expected relation, and, by comparing the results derived by emission-line fluxes to those inferred by PROSPECTOR, we corroborate that [O III] strengths are good tracers of ξ_{ion}. This is particularly useful in the high-redshift Universe, where Hydrogen recombination lines are not easily accessible.
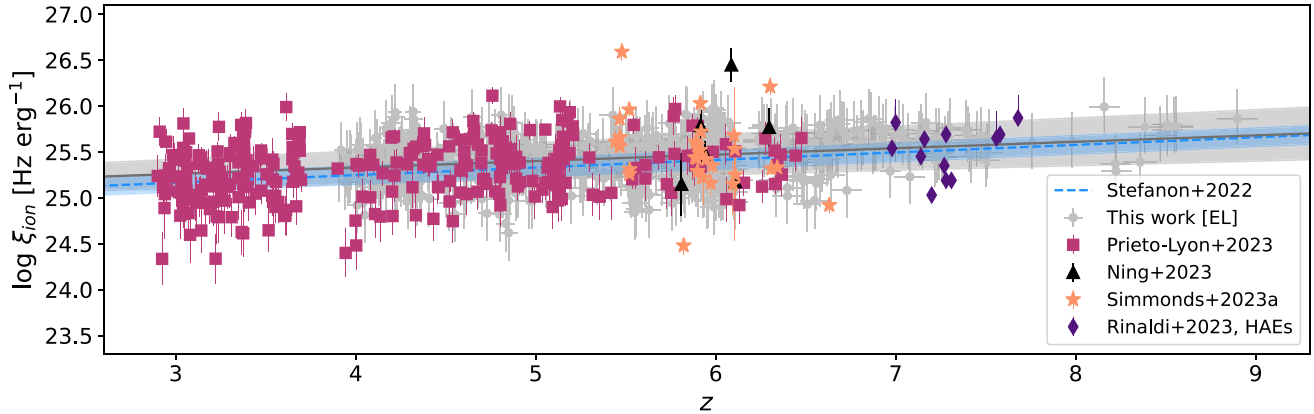
Figure 6. Comparison of ξ_{ion} inferred through photometrically estimated emission lines (grey circles and shaded area) with relevant values from literature, including the best-fitting line from Stefanon et al. (2022, blue dashed line and shaded area). In order of increasing redshift the comparison samples are: UV-faint galaxies at $z \sim 3$–7 from Prieto-Lyon et al. (2023, pink squares), LAEs from Ning et al. (2023, black triangles), and Simmonds et al. (2023, orange stars), and finally, the HAEs from Rinaldi et al. (2023a, purple diamonds). The agreement between this work and the previous ones in the field is remarkable. We note that the LAE with the highest ξ_{ion} from Simmonds et al. (2023) is hosting an AGN which is potentially boosting ξ_{ion}.
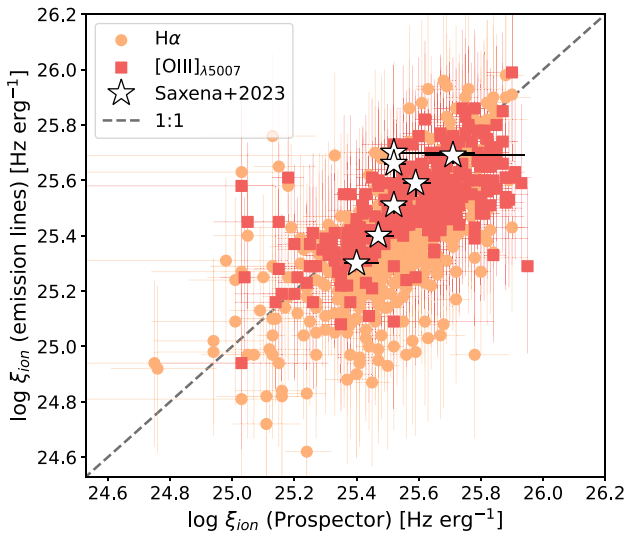

Figure 7. Comparison of ξ_{ion} inferred through Hα fluxes (orange circles) and [O III]$_{\lambda5007}$ EWs (red squares), with the values inferred by PROSPECTOR. We have also included the measurements from Saxena et al. (2023) as stars. The values scatter around the 1:1 relation, shown as a dashed grey line.

6 DISCUSSION

We begin by first addressing the biases that could potentially affect the results from this work. By construction, only galaxies with emission lines that can be measured from photometry were selected. Therefore, we are mostly focusing on star-forming galaxies. This was a necessary step in order to estimate ξ_{ion} from either Hα or [O III]. As an experiment, we used PROSPECTOR to fit a small subsample of galaxies with no obvious emission lines in the filter pairs of interest (*F335M*–*F356W* and *F410M*–*F444W*). As previously stated, PROSPECTOR does not rely on emission lines for the measurement of ξ_{ion}. We find that in these cases ξ_{ion} is consistently below 10^{25} Hz erg^{-1}, with values as low as 10^{23} Hz erg^{-1}, suggesting that there is a population of galaxies for which ξ_{ion} falls below the relation shown in Fig. 5, possibly explaining the origin of the trend

of ξ_{ion} with M_{UV}. This work is not representative of those galaxies, rather, it sheds light on the galaxies and mechanisms most likely responsible for reionizing the Universe. It must be noted that recent work by Looser et al. (2023a, b), among others, show that galaxies with no emission lines might be only temporarily quiescent, as a result of extremely bursty SFHs (Dome et al. 2024). Therefore, these kinds of galaxies are interesting to study (Katz et al. 2023), and are potentially important in the context of the EoR. The contribution of each galaxy population to the cosmic reionization budget is beyond the scope of this work, and will be presented in a future work, where the full capacity of JADES photometry will be combined with the power of PROSPECTOR to quantify the relative importance of different populations.

Using our sample, we now investigate the nature of the positive slope of ξ_{ion} with redshift, aiming to answer two questions: (1) is it physical or is it a result of our selection? and (2) If it is real, what is driving it?

6.1 Does ξ_{ion} evolve with redshift?

In order to answer this question we conduct a simple null-hypothesis test, shown in Fig. 10 (for simplicity, errors have been ignored in this test). We first select a subsample of galaxies at $z \sim 5.5$–6 from the galaxies used in this work, for which ξ_{ion} has been inferred through the [O III] EW (framed with a blue rectangle in the top panel). We assume that there is no evolution of ξ_{ion} with redshift, and that any observational study that says the contrary suffers from a luminosity bias (i.e. that at higher redshift we can only see the fainter galaxies with stronger emission lines). Under that assumption, we use our selected galaxies as seeds to produce 1000 simulated galaxies located randomly between $z \sim 5.5$–9, and that have been dimmed according to their luminosity distance (white circles with grey edges in middle panel). For these galaxies the rest-frame [O III] EWs estimated originally are used to obtain ξ_{ion} (see equation 3), so ξ_{ion} does not change with redshift for a specific seed. Finally, we apply the same selection criteria we did when constructing our sample, that is, a difference of 10 nJy between filter pairs (*F335M*–*F356W* or *F410M*–*F444W*). The galaxies deemed observable and that would be selected in our sample are shown as blue plus signs.

Table 2. Comparison between the ξ_{ion} values from this work to those presented in Saxena et al. (2023). The values estimated from emission-line fluxes and those derived from PROSPECTOR, are in broad agreement with those found through NIRSpec spectra. The columns are as in Table 1, but now include NIRSpec measurements.

Name	z	$\log \xi_{\text{ion, 0}}$ (Hα) [Hz erg^{-1}]	$\log \xi_{\text{ion}}$ ([O III]) [Hz erg^{-1}]	$\log \xi_{\text{ion}}$ (PROSPECTOR) [Hz erg^{-1}]	$\log \xi_{\text{ion}}$ (NIRSpec) [Hz erg^{-1}]
JADES-GS $+$ 53.17657$-$27.77113	5.89 ± 0.07	–	$25.58^{+0.11}_{-0.15}$	$25.52^{+0.04}_{-0.03}$	$25.66^{+0.05}_{-0.05}$ (Hα)
JADES-GS $+$ 53.12176$-$27.79764	5.93 ± 0.14	$25.57^{+0.20}_{-0.40}$	$25.54^{+0.11}_{-0.15}$	$25.52^{+0.01}_{-0.00}$	$25.70^{+0.01}_{-0.01}$ (Hα)
JADES-GS $+$ 53.11042$-$27.80892	5.94 ± 0.06	$25.10^{+0.20}_{-0.40}$	$25.43^{+0.11}_{-0.15}$	$25.40^{+0.07}_{-0.04}$	$25.30^{+0.02}_{-0.02}$ (Hα)
JADES-GS $+$ 53.16062$-$27.77161	5.97 ± 0.07	–	$25.46^{+0.11}_{-0.15}$	$25.52^{+0.04}_{-0.03}$	$25.51^{+0.03}_{-0.03}$ (Hα)
JADES-GS $+$ 53.13492$-$27.77271	6.33 ± 0.09	$25.19^{+0.20}_{-0.40}$	$25.60^{+0.20}_{-0.40}$	$25.47^{+0.05}_{-0.04}$	$25.40^{+0.02}_{-0.02}$ (Hα)
JADES-GS $+$ 53.16905$-$27.77883	6.63 ± 0.08	–	$25.47^{+0.20}_{-0.40}$	$25.71^{+0.23}_{-0.09}$	$25.69^{+0.03}_{-0.04}$ (Hα)
JADES-GS $+$ 53.15683$-$27.76716	7.98 ± 0.10	–	$25.62^{+0.20}_{-0.40}$	$25.59^{+0.05}_{-0.04}$	$25.59^{+0.05}_{-0.05}$ (Hβ)

Notes. Column 1: JADES identifier, composed of the coordinates of the centroid rounded to the fifth decimal place, in units of degrees. Column 2: photometric redshift inferred using the template-fitting code EAZY. Columns 3–6: logarithm of the ionizing photon production efficiency estimations in units of Hz erg^{-1}. For the NIRSpec estimations, we specify whether Hα or Hβ fluxes were used to infer ξ_{ion}.
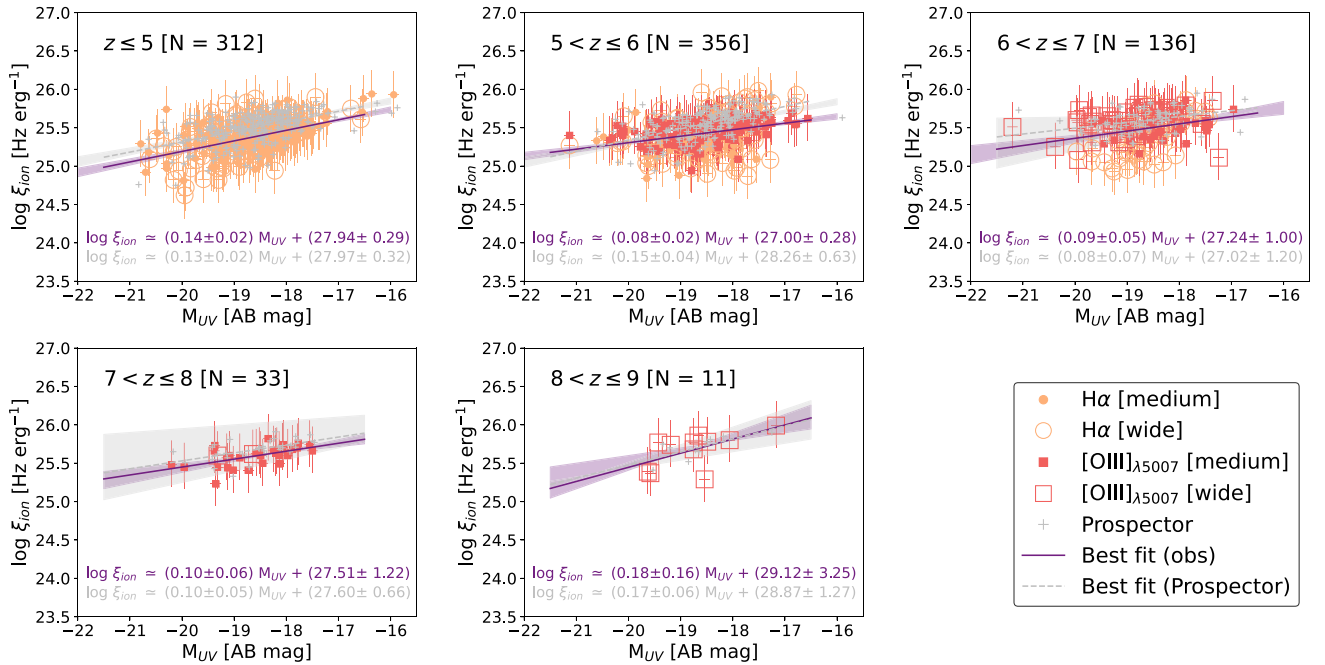

Figure 8. Dependence of ξ_{ion} on UV magnitude, separated in redshift bins. The symbols and colours are the same as in Figs 4 and 8. The number of galaxies in each redshift bin is indicated in the top left corner of each panel. The filled (dashed) line is the best fit to the data obtained via emission lines (PROSPECTOR). We find that fainter galaxies are more efficient at producing ionizing radiation, as expected from previous studies. The discrepancy between the best fit lines at $5 \leq z \leq 6$ is driven by underestimated Hα flux estimations, this emission line falls largely on the *F444W* band in this redshift bin, where the measurements are less accurate. A version of this figure with $\dot{n}_{\text{ion}}$ can be found in Appendix B.

The ξ_{ion} slope derived through emission-line fluxes is shown in all panels as a dashed blue line, whereas the slope obtained after this test is shown in red. It is clear that these slopes do not match and that the red slope is flat. From this exercise, we can conclude that the increase of ξ_{ion} with redshift is not mainly due to our selection criteria. Furthermore, we investigate the possibility of a stellar mass bias driving the observed ξ_{ion} evolution with redshift. In the bottom panel, we conduct a similar experiment as the one just described, but now using as seeds the galaxies in our sample with low stellar masses ($\log M/\text{M}_{\odot} < 8.0$; shown as purple crosses in the top panel), it is important to note that in our sample, this is equivalent to studying galaxies fainter than $M_{\text{UV}} \simeq -19$. We find that lower mass (fainter) galaxies have higher ξ_{ion}, but that this property alone is insufficient in

explaining the increase of ξ_{ion} with redshift. Therefore, we go forward under the assumption that, even if there is a degree of observational bias, there is a physical cause driving the observed ξ_{ion} evolution with redshift.

6.2 What drives the ξ_{ion} evolution?

We now aim to investigate the main driver of the observed increase of ξ_{ion} with redshift. Throughout this paper, we have demonstrated that our simple prescription to measure line fluxes from photometry is adequate, agreeing with both NIRSpec and FRESCO grism flux measurements (when available). We have also shown that our ξ_{ion} values agree with those found in the literature, and finally, with
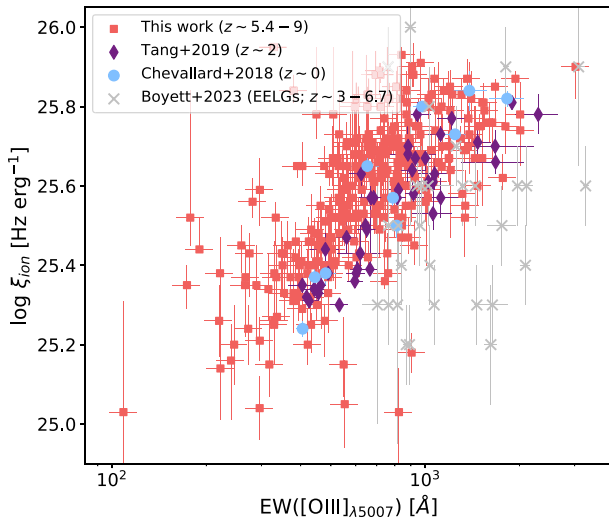
Figure 9. ξ_{ion} versus $[O \, III]_{\lambda5007}$ EWs (figure adapted from Tang et al. 2019). The red squares represent our sample, described by $\log \xi_{ion} = (0.57 \pm 0.09) \times \log(EW[[O \, III]_{\lambda5007}]) + (23.97 \pm 0.25)$, while the purple diamonds show the results from Tang et al. (2019), and the light blue circles those from Chevallard & Charlot (2016). We also include the EELGs from Boyett et al. (in preparation) as grey crosses. The ξ_{ion} for our sample is provided by PROSPECTOR. Except for a few outliers, our sample follows the same trend as the previous works, confirming that $[O \, III]$ strength is also a reliable tracer of ξ_{ion} in the early Universe.

those inferred with PROSPECTOR. We now focus particularly on this last point, and exploit the synergy between observations and SED fitting to find which galactic property (or properties) is (are) driving the ξ_{ion} evolution. For this purpose we calculate a Spearman's rank correlation coefficient for ξ_{ion} against the following properties: redshift, stellar mass, UV magnitude (both observed and intrinsic), recent SFR (SFR$_{10}$; in the past 10 Myr), SFR in the past 100 Myr (SFR$_{100}$), stellar metallicity, ionization parameter, dust index (dust2 in the prescription of Conroy et al. 2009), half-mass assembly time (t50), and ionizing photons emitted per second ($\dot{n}_{ion}$). All of the results are shown in Appendix A, with their correlation and p-value shown in the title of each panel. An excerpt of the table containing all the values can be found in Table A1.

We find that in our sample ξ_{ion} correlates with M_{UV}, half-mass stellar age, and metallicity, however, the strongest correlations are those of ξ_{ion} with stellar mass, where lower masses lead to higher ξ_{ion} values, and with SFR. Motivated by these findings, we explore the correlation of ξ_{ion} with the SFH burstiness, which translates into the ratio between both recent and older SFR (SFR$_{10}$/SFR$_{100}$). Fig. 11 shows how burstiness becomes increasingly important at lower stellar masses, and that low-mass galaxies with bursty star formation have the highest ξ_{ion} values in the sample. Also shown is the correlation between stellar mass and M_{UV}, and recent star formation versus stellar mass (colour-coded by ξ_{ion} and $\dot{n}_{ion}$, respectively). The Spearman's correlation coefficient value for SFR$_{10}$/SFR$_{100}$ is 0.914, with a p-value consistent with zero, indicating a strong positive correlation between ξ_{ion} and burstiness of the SFH. Therefore, from PROSPECTOR, we conclude that low mass and burstiness in a galaxy are the most important properties driving ξ_{ion}. It is important to note that although low-mass galaxies have a higher ξ_{ion}, they do not have a correspondingly higher $\dot{n}_{ion}$ than higher mass galaxies. In fact, since $\dot{n}_{ion}$ is the net ionizing photon flux of a galaxy, it has the opposite
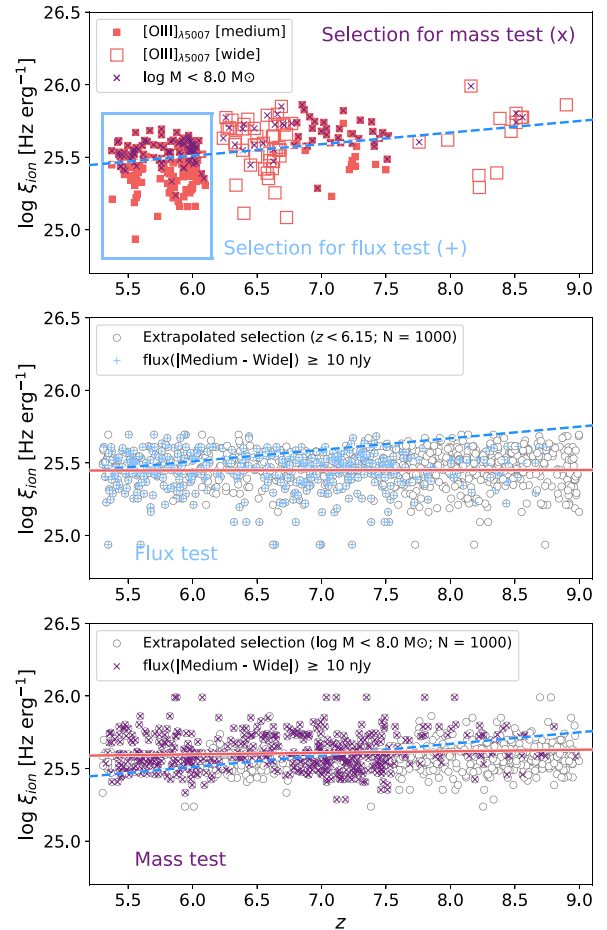

Figure 10. Null hypothesis test. ξ_{ion} versus redshift, the blue dashed line (in all panels) is the best fit to the ξ_{ion} inferred via emission lines, as seen in Fig. 5. For simplicity, errors have been omitted. Top panel: ξ_{ion} values from this work, obtained via $[O \, III]$ EWs. The blue rectangle shows the galaxies selected as seeds in order to simulate 1000 galaxies covering the whole redshift range shown ($z \sim 5.5$–9) in the middle panel. While the purple crosses mark the galaxies that have low stellar masses ($\log M < 8.0 \, M_\odot$), and are used as seeds to simulate 1000 galaxies in the bottom panel. Middle panel: simulated galaxies (white circles with grey edges) and ones that would be observable according to our sample selection criteria (blue plus signs; flux difference between filter pairs of at least 10 nJy). Bottom panel: simulated galaxies (white circles with grey edges) and ones that would be observable according to our sample selection criteria (purple crosses; flux difference between filter pairs of at least 10 nJy). The red solid line in the middle and bottom panels is the best fit to the blue plus signs and purple crosses, respectively. The slope of the red line does not match the slope of the blue dashed one, indicating that the null hypothesis is wrong in both cases, and that the increase of ξ_{ion} with redshift is not due to a luminosity or mass bias in our selection criteria.

behaviour (see Appendix B). ξ_{ion} represents the ratio between the ionizing photons that are being produced ($\dot{n}_{ion}$) and the non-ionizing UV continuum, the latter not only includes contributions from young stellar populations, but also from older ones. Low-mass galaxies tend to be dominated by younger stellar populations, and thus, the increase in ξ_{ion} is not due to a higher number of ionizing photons being emitted, but due to a relative lack of UV continuum.

Burstiness in star formation is usually associated with low stellar masses (Weisz et al. 2012; Guo et al. 2016), mainly due to stellar feedback. In brief, supernovae occurring after intense star formation
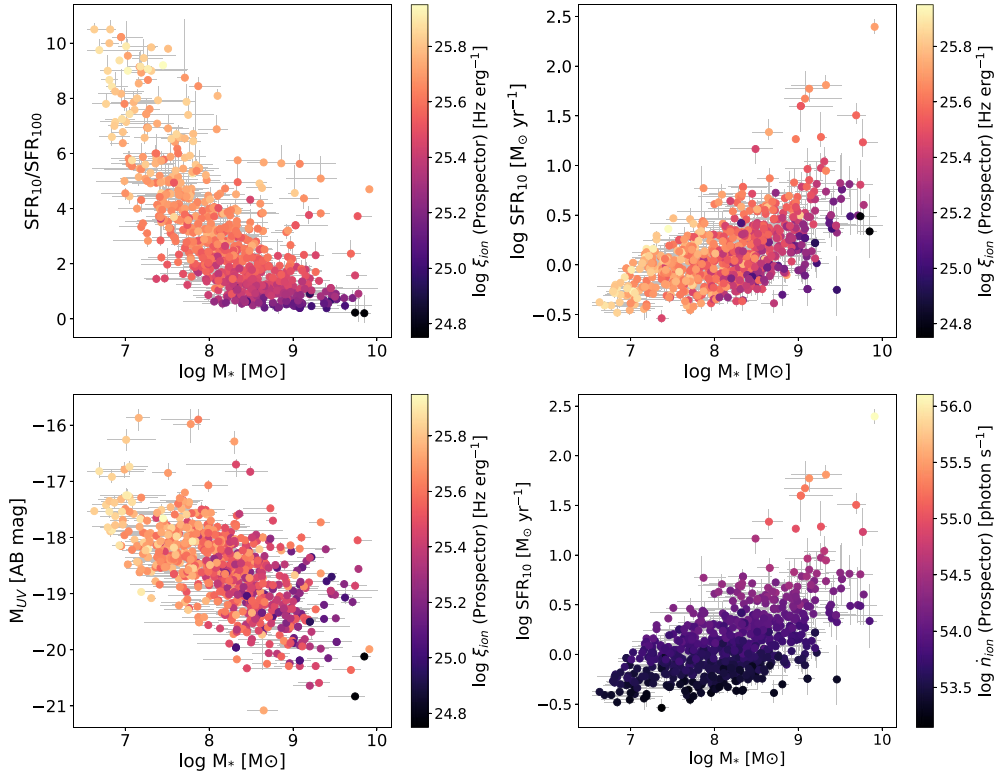
Figure 11. Relations between relevant galactic properties, as inferred by PROSPECTOR. Top left panel: ratio between recent (within 10 Myr) and sustained over 100 Myr star formation, SFR_{10}/SFR_{100} (i.e. burstiness of star formation), over stellar mass, and colour-coded by ξ_{ion}. The Spearman's rank correlation coefficient value is 0.914, while the *p*-value is consistent with zero. Lower mass galaxies with bursty SFHs have an increased ξ_{ion} with respect to non-bursty higher-mass galaxies. Bottom left panel: correlation between UV luminosity and stellar mass, colour-coded by ξ_{ion}. There is a strong trend of decreasing stellar mass with increasing M_{UV}. Top and bottom right panels: relation between recent star formation, stellar mass and ξ_{ion} (top) or $\dot{n}_{ion}$ (bottom).

heat up and expel gas. This leads to star formation being temporarily quenched (Stinson et al. 2007; Dome et al. 2024), followed by new gas accretion, which results in new star-forming episodes. Burstiness in high-redshift galaxies can also be explained by their dynamical time-scale, which becomes too short for supernovae feedback to respond to gravitational collapse (Faucher-Giguère 2018; Tacchella, Forbes & Caplar 2020). At high redshift, galaxies with low stellar masses are expected to be more numerous (Bouwens et al. 2015, 2023; Austin et al. 2023; Harikane et al. 2023). Additionally, these types of galaxies are thought to be the main sources responsible for reionizing the Universe (Hassan et al. 2018; Rosdahl et al. 2018; Trebitsch et al. 2020). In a recent work, Atek et al. (2023) present spectroscopic observations of extremely low-mass lensed galaxies ($\log M/M_\odot \sim 6$–7) with high ξ_{ion} ($\log \xi_{ion}/Hz\, erg^{-1} \sim 25.8$, measured through the H$\alpha$ recombination line). These kinds of galaxies are likely key in the reionization of the Universe. Our results support the scenario of low-mass galaxies being efficient producers of ionizing radiation, in agreement with previous findings.

6.3 The impact of ξ_{ion} on the cosmic ionization budget

We first study how the number of ionizing photons produced per volume unit, $\dot{N}_{ion}$, varies with M_{UV} and redshift. We adopt the UV luminosity functions from Bouwens et al. (2021), and two different prescriptions for f_{esc}: constant (of 10 per cent and 20 per cent, Ouchi et al. 2009; Robertson et al. 2013, 2015), and varying with M_{UV}. For the variable prescription, we follow the work of Anderson et al. (2017), who estimate f_{esc} over a large range of galaxy masses,

using the high-resolution, uniform volume simulation Vulcan. This simulation provides detailed distributions of gas and stars in resolved galaxies, allowing precise measurements of f_{esc}. Anderson et al. (2017) find a dependence of f_{esc} with M_{UV} given by: $\log f_{esc} = (0.51 \pm 0.4)M_{UV} + 7.3 \pm 0.08$. For ξ_{ion}, we assume the best-fitting lines to our observations given in Fig. 8. It is important to mention that by following this prescription we are assuming that the ξ_{ion} evolution is representative for all low-mass faint galaxies, when in fact, it does not represent galaxies in quiescent phases (without detectable emission lines). Therefore, the cosmic ionizing photon budgets here derived should be taken as upper limits. In a future work, we will quantify the contribution of different galaxy populations to reionization, and these calculations will be further constrained.

The $\dot{N}_{ion}$ results as a function of M_{UV} are presented in Fig. 12, where each panel shows a different escape fraction. At every redshift bin, the fainter galaxies dominate the budget of cosmic reionization. In particular, that galaxies fainter than $M_{UV} \sim -19$ account for at least 90 per cent of the total $\dot{N}_{ion}$. This is especially true for the case with the variable f_{esc} from (Anderson et al. 2017), where $\dot{N}_{ion}$ has a steeper dependence with M_{UV}, and galaxies fainter than $M_{UV} = -18$ account for more than 90 per cent of the total ionizing budget at all redshift bins. It is important to mention that the curves start to flatten at $M_{UV} \sim -20$ for the constant f_{esc} cases, which means that faint (but not necessarily extremely faint) galaxies are significant contributors to reionization. If we use the same luminosity functions but instead adopt a constant ξ_{ion} value of $\log \xi_{ion} = 25.2$ Hz erg^{-1} (motivated by stellar populations, as in Robertson et al. 2013), and a constant f_{esc} of 10 per cent (seen as black shaded area in top panel), we find
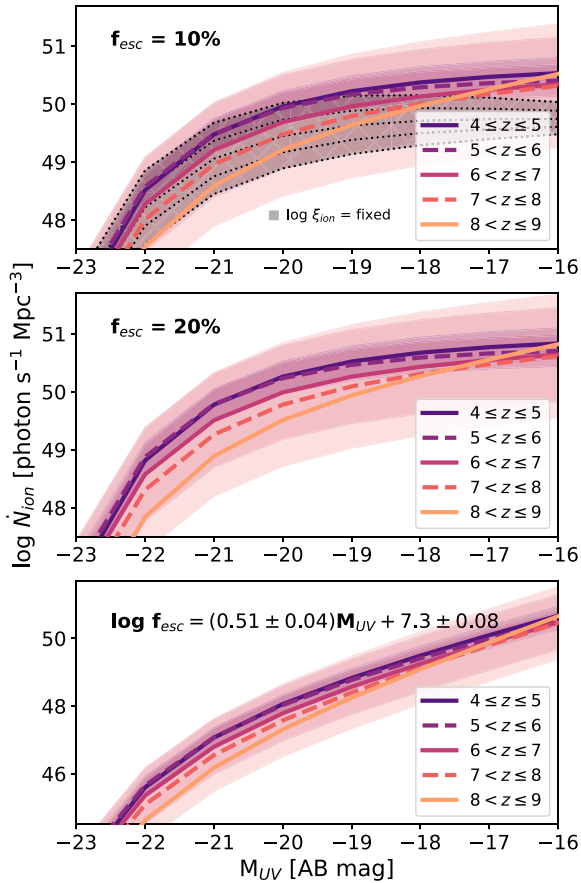
Figure 12. $\dot{N}_{\mathrm{ion}}$ as a function of M_{UV}, by redshift bins, assuming a f_{esc} indicated in each panel and a ξ_{ion} described by our data. The prescription of f_{esc} that varies with M_{UV} was taken from Anderson et al. (2017), while the UV luminosity functions were adopted from Bouwens et al. (2021), for the redshifts relevant to this work. For comparison, in the top panel, results adopting a constant $\log \xi_{\mathrm{ion}} = 25.2$ Hz erg^{-1} are shown in black. At every redshift and for every f_{esc}, galaxies fainter than $M_{\mathrm{UV}} \sim -19$ dominate the ionization budget, indicating that faint (but not necessarily extremely faint) galaxies contribute significantly to reionization.

that at the highest redshift bin investigated ($z = 8$–9) our results are significantly higher, and can translate to a reduction in the average f_{esc} from 10 per cent to ~ 2 per cent. This is a natural result of a ξ_{ion} dependant on both galaxy mass and redshift (Finkelstein et al. 2019).

Using the curves derived in the previous step, we now investigate the effect of our ξ_{ion} estimation in the evolution of the cosmic ionization budget, $\dot{N}_{\mathrm{ion}}$ with redshift, given by:

$$\dot{N}_{\mathrm{ion}}(z) = f_{\mathrm{esc}} \times \xi_{\mathrm{ion}}(z) \times \rho_{\mathrm{UV}}(z), \qquad (5)$$

where $\dot{N}_{\mathrm{ion}}$ is in units of photon s^{-1} Mpc^{-3}, ξ_{ion} is in units of Hz erg^{-1}, and ρ_{UV} in units of erg s^{-1} Hz^{-1} Mpc^{-3}. The escape fraction is dimensionless and can be assumed constant. In addition to the (Bouwens et al. 2021) luminosity functions, we now include the red solid curve provided in fig. 7 of Sun & Furlanetto (2016), which fits a power law to the low-mass end. To estimate ξ_{ion}, we use the equation that describes the best fit to our data (see Fig. 5), and assume f_{esc} values of 10 per cent and 20 per cent, in accordance to the canonical average f_{esc} values needed for galaxies to be capable of ionizing the Universe (Ouchi et al. 2009; Robertson et al. 2013, 2015). In addition, we integrate the curves from Fig. 12 down to $M_{\mathrm{UV}} =$
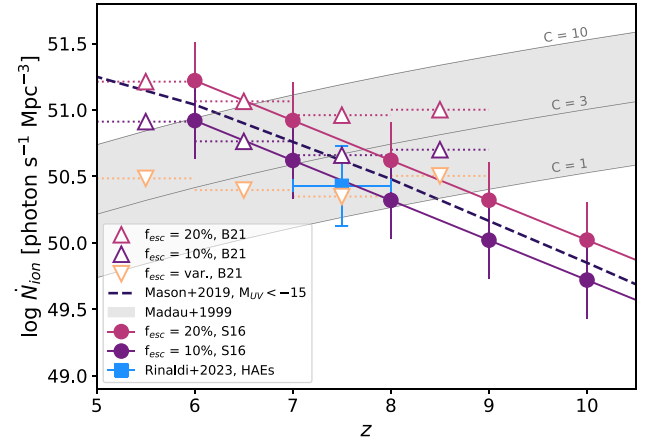

Figure 13. Cosmic rate of ionizing photons being emitted per second and per unit of volume, $\dot{N}_{\mathrm{ion}}$, as a function of redshift, assuming a f_{esc} as indicated, and a ξ_{ion} described by our data (i.e. $\log \xi_{\mathrm{ion}} = (0.07 \pm 0.02)z + 25.05 \pm 0.11$). We show the results obtained when adopting the UV luminosity density from Sun & Furlanetto (2016, circles labelled 'S16'), as well as results obtained by integrating the UV luminosity density curves from Bouwens et al. (2021) down to $M_{\mathrm{UV}} = -16$ (triangles labelled 'B21', curves shown in Fig. 12). As comparison, we include the curve from Mason et al. (2015) assuming constant ξ_{ion} and f_{esc}, integrated down to an M_{UV} of -15 (as in Mason et al. 2019), as well as the $\dot{N}_{\mathrm{ion}}$ reported in Rinaldi et al. (2023a) for HAEs at $z \sim 7$–8 (blue square). Finally, we include the estimated $\dot{N}_{\mathrm{ion}}$ needed to maintain Hydrogen ionization in the IGM (Madau et al. 1999), adopting clumping factors of 1, 3, and 10. We find a cosmic $\dot{N}_{\mathrm{ion}}$ consistent with literature up to $z \sim 8$, but that starts to rise at the highest redshift bin due to the dependence of ξ_{ion} with M_{UV}.

-16, and show the results as open triangles in Fig. 13. The values adopting the variable ξ_{ion} from this work (triangles) are consistent with those from literature up to $z \sim 8$ (e.g. Bouwens et al. 2015; Mason, Trenti & Treu 2015; Mason et al. 2019; Naidu et al. 2020; Rinaldi et al. 2023a). However, there is an upturn in the last redshift bin, where faint low-mass galaxies dominate and the ξ_{ion} dependence with M_{UV} and redshift becomes more important. As comparison, we add the estimated $\dot{N}_{\mathrm{ion}}$ that is required to maintain the ionization of Hydrogen according to the models of (Madau, Haardt & Rees 1999), adopting clumping factors of 1, 3, and 10. A clumping factor of unity represents a uniform IGM, whereas larger clumping factors imply that an increased number of recombinations are taking place in the IGM. This leads to the need for a higher number of ionizing photons to be produced, in order to reach a balance between ionization and recombination rates. If the ξ_{ion} derived in this work is representative of the faint low-mass galaxy population, then these kind of galaxies would produce an ionizing photon budget sufficient to ionize the Universe by the end of the EoR.

6.4 Implications for reionization

The connection between the cosmic $\dot{N}_{\mathrm{ion}}$ estimations and our previous conclusions comes through the stellar mass of galaxies. Stellar mass has been seen to decrease as galaxies become fainter, for example, Bhatawdekar et al. (2019) analyse this relation at $z = 6$–9 using data from the Hubble Frontier Fields. They notice that despite seeing a few high-mass galaxies with faint UV luminosities, there is a clear trend (with a large scatter) of stellar mass decreasing as galaxies become fainter in M_{UV} (see also; Song et al. 2016). In particular, galaxies fainter than $M_{\mathrm{UV}} \sim -18$ have stellar masses

below $\sim 10^8$ M$_\odot$. In our sample, galaxies with comparable mass have the highest $\xi_{\rm ion}$, which is illustrated in Fig. 11, where we also show the correlation between stellar mass and $M_{\rm UV}$. Therefore, the conclusions made from estimating the cosmic ionizing photon budget agree with the ones drawn from combining our emission-line estimations with PROSPECTOR. In particular, that low-mass galaxies in the fainter end of luminosity functions are more efficient in producing ionizing radiation, and might be the main drivers of reionization. This conclusion has also been reached independently by use of the THESAN project (Kannan et al. 2022), a suite of radiation-magnetohydrodynamic simulations of the EoR. Specifically, Yeh et al. (2023) find that galaxies in THESAN with low stellar masses (M_* $\leq 10^7$M$_\odot$) drive reionization above $z \sim 7$. As mentioned previously, this conclusion depends on how representative our sample is of the general galaxy population, and how common low-mass bursty galaxies in a quiescent phase are, both topics to be presented in a future study. Promisingly, Rinaldi et al. (2023a) find that Hα emitters (HAEs) contribute significantly more to $\dot{N}_{\rm ion}$ than their non-Hα emitting counterparts, for a sample of galaxies at $z \sim 7$–8.

In brief, based on our sample of galaxies with detectable Hα and/or [O III] emission lines, we conclude that the increase of $\xi_{\rm ion}$ with redshift in this population is likely physical in origin. The main driver of the observed evolution is the stellar mass of galaxies, which leads to bursty SFHs and result in higher $\xi_{\rm ion}$ (and possibly higher $f_{\rm esc}$). Additionally, we convolve our $\xi_{\rm ion}$ estimations with UV luminosity functions from literature, and find that if our findings are representative of the faint low-mass galaxy population, then these galaxies can produce enough ionizing photons to ionize the Universe by the end of the EoR. In particular, we find that the $\xi_{\rm ion}$ relations found in this work can reduce the requirement of average escape fractions, if assumed constant, to <10 per cent. The effect is more significant at higher redshifts where faint low-mass galaxies dominate luminosity functions.

7 CONCLUSIONS

In summary, we use NIRCam Deep imaging to build a sample of 677 galaxies at $z = 3.9$–8.9, for which Hα and/or [O III]$_{\lambda 5007}$ fluxes can be estimated from photometry. By construction, this sample does not include galaxies in quiescent phases. Depending on the redshift, we estimate $\xi_{\rm ion}$ through Hα and/or EW([O III]$_{\lambda 5007}$), measured from photometry in the filter pairs: $F335M$–$F356W$ and $F410M$–$F444W$. We adopt an SMC dust attenuation curve, proven to be adequate at high redshifts. Simultaneously, we fit all the photometry with PROSPECTOR and derive $\xi_{\rm ion}$, in addition to relevant galaxy properties. The $\xi_{\rm ion}$ measurements inferred through emission-line fluxes agree with the values derived by PROSPECTOR. We find that $\xi_{\rm ion}$ evolves with both redshift and $M_{\rm UV}$, and this evolution is not only due to observational biases. To place our results on a cosmic scale, we combine our relations of $\xi_{\rm ion}$ with redshift and $M_{\rm UV}$, along with two different $f_{\rm esc}$ treatments: constant (10 per cent and 20 per cent), and variable as a function of $M_{\rm UV}$, to constrain the cosmic budget of reionization, $\dot{N}_{\rm ion}$, and make conclusions about which kind of galaxies dominate this budget. The main conclusions of this work are the following:

(i) By comparing the resulting $\xi_{\rm ion}$ using [O III] EWs with those inferred by PROSPECTOR, we confirm the effectiveness of EW([O III]) to estimate $\xi_{\rm ion}$ in the high-redshift Universe.

(ii) For our sample, $\xi_{\rm ion}$ evolves positively with redshift as: $\log \xi_{\rm ion} = (0.07 \pm 0.02)z + (25.05 \pm 0.11)$.

(iii) We perform a two-dimensional fit to account for the evolution of $\xi_{\rm ion}$ with both redshift and $M_{\rm UV}$, and find: $\log \xi_{\rm ion}(z, M_{\rm UV}) = (0.05 \pm 0.02)z + (0.11 \pm 0.02)M_{\rm UV} + (27.33 \pm 0.37)$.

(iv) The observed evolution of $\xi_{\rm ion}$ is likely has a physical origin, and is driven by specific SFR of galaxies. Specifically, lower mass leads to burstier SFHs, which we find is the property that has the strongest correlation with $\xi_{\rm ion}$.

(v) By comparing $\dot{N}_{\rm ion}$ obtained by adopting a constant $f_{\rm esc}$ of 10 per cent and a constant ionizing photon production efficiency of $\log \xi_{\rm ion}/[{\rm Hz~erg}^{-1}] = 25.2$, with our evolving $\xi_{\rm ion}$ prescriptions, we conclude that the average $f_{\rm esc}$ requirement can be reduced to <10 per cent, an effect that increases with redshift (as low as ~ 2 per cent for our highest redshift bin).

(vi) If our sample is representative of faint low-mass galaxies, then these kind of galaxies can account for the budget of ionizing photons required to ionize the Universe by the end of the EoR.

In this study, we conclude that low-mass faint galaxies with bursty SFHs are efficient enough in producing ionizing photons to be the main sources responsible for ionizing the Universe. We note that the sample used in this work was constructed to have detectable emission lines, particularly, Hα and/or [O III]$_{\lambda 5007}$, and is therefore not representative of every galaxy population. However, the population here studied is likely representative of the galaxies responsible for ionizing the Universe. In a future study, we will use the full potential of JADES photometry to shed light on the contribution different galaxy populations have to the total cosmic ionizing budget.

University, Institute for Data Intensive Engineering and Science (IDIES).

DATA AVAILABILITY

The data underlying this article will be shared on reasonable request to the corresponding author.

REFERENCES

Anderson L., Governato F., Karcher M., Quinn T., Wadsley J., 2017, MNRAS, 468, 4077

Atek H., Furtak L. J., Oesch P., van Dokkum P., Reddy N., Contini T., Illingworth G., Wilkins S., 2022, MNRAS, 511, 4464

Atek H. et al., 2023, preprint (arXiv:2308.08540)

Austin D. et al., 2023, ApJ, 952, L7

Becker R. H. et al., 2001, AJ, 122, 2850

Beckwith S. V. W. et al., 2006, AJ, 132, 1729

Bhatawdekar R., Conselice C. J., Margalef-Bentabol B., Duncan K., 2019, MNRAS, 486, 3805

Bian F., Fan X., McGreer I., Cai Z., Jiang L., 2017, ApJ, 837, L12

Borthakur S., Heckman T. M., Leitherer C., Overzier R. A., 2014, Science, 346, 216

Bosman S. E. I. et al., 2022, MNRAS, 514, 55

Bouwens R. J. et al., 2015, ApJ, 803, 34

Bouwens R. J., Smit R., Labbé I., Franx M., Caruana J., Oesch P., Stefanon M., Rasappu N., 2016, ApJ, 831, 176

Bouwens R. J. et al., 2021, AJ, 162, 47

Bouwens R. J. et al., 2023, MNRAS, 523, 1036

Bowler R. A. A., Bourne N., Dunlop J. S., McLure R. J., McLeod D. J., 2018, MNRAS, 481, 1631

Bowler R. A. A., Cullen F., McLure R. J., Dunlop J. S., Avison A., 2022, MNRAS, 510, 5088

Boyett K. N. K., Stark D. P., Bunker A. J., Tang M., Maseda M. V., 2022, MNRAS, 513, 4451

Bradley L. et al., 2022, astropy/photutils: 1.5.0, Zenodo, available at: https://doi.org/10.5281/zenodo.6825092

Brammer G. B., van Dokkum P. G., Coppi P., 2008, ApJ, 686, 1503

Bunker A. J., Warren S. J., Hewett P. C., Clements D. L., 1995, MNRAS, 273, 513

Byler N., Dalcanton J. J., Conroy C., Johnson B. D., 2017, ApJ, 840, 44

Calzetti D., Kinney A. L., Storchi-Bergmann T., 1994, ApJ, 429, 582

Cameron A. J. et al., 2023, A&A, 677, 115

Carnall A. C., McLure R. J., Dunlop J. S., Davé R., 2018, MNRAS, 480, 4379

Chabrier G., 2003, PASP, 115, 763

Charlot S., Longhetti M., 2001, MNRAS, 323, 887

Chevallard J., Charlot S., 2016, MNRAS, 462, 1415

Chevallard J. et al., 2018, MNRAS, 479, 3264

Conroy C., Gunn J. E., White M., 2009, ApJ, 699, 486

De Barros S., Oesch P. A., Labbé I., Stefanon M., González V., Smit R., Bouwens R. J., Illingworth G. D., 2019, MNRAS, 489, 2355

Dome T., Tacchella S., Fialkov A., Dekel A., Ginzburg O., Lapiner S., Looser T. J., 2024, MNRAS, 527, 2139

Duncan K., Conselice C. J., 2015, MNRAS, 451, 2030

Eisenstein D. J. et al., 2023, preprint (arXiv:2306.02465)

Eldridge J. J., Stanway E. R., Xiao L., McClelland L. A. S., Taylor G., Ng M., Greis S. M. L., Bray J. C., 2017, Publ. Astron. Soc. Aust., 34, e058

Emami N., Siana B., Alavi A., Gburek T., Freeman W. R., Richard J., Weisz D. R., Stark D. P., 2020, ApJ, 895, 116

Endsley R., Stark D. P., Chevallard J., Charlot S., 2021, MNRAS, 500, 5229

Faisst A. L. et al., 2016, ApJ, 821, 122

Faisst A. L., Capak P. L., Emami N., Tacchella S., Larson K. L., 2019, ApJ, 884, 133

Fan X. et al., 2006, AJ, 131, 1203

Faucher-Giguère C.-A., 2018, MNRAS, 473, 3717

Ferland G. J. et al., 2013, Rev. Mex. Astron. Astrofis., 49, 137

Ferland G. J. et al., 2017, Rev. Mex. Astron. Astrofis., 53, 385

Finkelstein S. L. et al., 2019, ApJ, 879, 36

Flury S. R. et al., 2022, ApJS, 260, 1

Gallerani S. et al., 2010, A&A, 523, A85

Gardner J. P. et al., 2023, PASP, 135, 068001

Giavalisco M. et al., 2004, ApJ, 600, L93

Gordon K. D., Clayton G. C., 1998, ApJ, 500, 816

Gordon K. D., Clayton G. C., Misselt K. A., Landolt A. U., Wolff M. J., 2003, ApJ, 594, 279

Guo Y. et al., 2016, ApJ, 833, 37

Hainline K. N. et al., 2023, preprint (arXiv:2306.02468)

Harikane Y. et al., 2018, ApJ, 859, 84

Harikane Y. et al., 2023, ApJS, 265, 5

Hassan S., Davé R., Mitra S., Finlator K., Ciardi B., Santos M. G., 2018, MNRAS, 473, 227

Izotov Y. I., Worseck G., Schaerer D., Guseva N. G., Chisholm J., Thuan T. X., Fricke K. J., Verhamme A., 2021, MNRAS, 503, 1734

Johnson B. D., Leja J. L., Conroy C., Speagle J. S., 2019, Astrophysics Source Code Library, record ascl:1905.025

Johnson B. D., Leja J., Conroy C., Speagle J. S., 2021, ApJS, 254, 22

Kannan R., Garaldi E., Smith A., Pakmor R., Springel V., Vogelsberger M., Hernquist L., 2022, MNRAS, 511, 4005

Katz H. et al., 2023, MNRAS, 518, 270

Keating L. C., Weinberger L. H., Kulkarni G., Haehnelt M. G., Chardin J., Aubert D., 2020, MNRAS, 491, 1736

Lam D. et al., 2019, A&A, 627, A164

Leitet E., Bergvall N., Hayes M., Linné S., Zackrisson E., 2013, A&A, 553, A106

Leitherer C., Hernandez S., Lee J. C., Oey M. S., 2016, ApJ, 823, 64

Leja J., Carnall A. C., Johnson B. D., Conroy C., Speagle J. S., 2019, ApJ, 876, 3

Looser T. J. et al., 2023a, preprint (arXiv:2302.14155)

Looser T. J. et al., 2023b, preprint (arXiv:2306.02470)

Lovell C. C., Vijayan A. P., Thomas P. A., Wilkins S. M., Barnes D. J., Irodotou D., Roper W., 2021, MNRAS, 500, 2127

Ma X. et al., 2019, MNRAS, 487, 1844

Madau P., 1995, ApJ, 441, 18

Madau P., Haardt F., Rees M. J., 1999, ApJ, 514, 648

Maiolino R., Mannucci F., 2019, A&AR, 27, 3

Maiolino R. et al., 2023, preprint (arXiv:2308.01230)

Mármol-Queraltó E., McLure R. J., Cullen F., Dunlop J. S., Fontana A., McLeod D. J., 2016, MNRAS, 460, 3587

Maseda M. V. et al., 2020, MNRAS, 493, 5120

Mason C. A., Trenti M., Treu T., 2015, ApJ, 813, 21

Mason C. A., Naidu R. P., Tacchella S., Leja J., 2019, MNRAS, 489, 2669

Matthee J., Sobral D., Darvish B., Santos S., Mobasher B., Paulino-Afonso A., Röttgering H., Alegre L., 2017, MNRAS, 472, 772

Naidu R. P., Tacchella S., Mason C. A., Bose S., Oesch P. A., Conroy C., 2020, ApJ, 892, 109

Naidu R. P. et al., 2022, MNRAS, 510, 4582

Nakajima K., Ellis R. S., Iwata I., Inoue A. K., Kusakabe H., Ouchi M., Robertson B. E., 2016, ApJ, 831, L9

Nanayakkara T. et al., 2020, ApJ, 889, 180

Ning Y., Cai Z., Jiang L., Lin X., Fu S., Spinoso D., 2023, ApJ, 944, L1

Oesch P. A. et al., 2023, MNRAS, 525, 2864

Onodera M. et al., 2020, ApJ, 904, 180

Osterbrock D. E., Ferland G. J., 2006, Astrophysics of Gaseous Nebulae and Active Galactic Nuclei. University Science Books, Sausalito, CA

Ouchi M. et al., 2009, ApJ, 706, 1136

Paardekooper J.-P., Khochfar S., Dalla Vecchia C., 2015, MNRAS, 451, 2544

Pannella M. et al., 2015, ApJ, 807, 141

Planck Collaboration XLVII, 2016, A&A, 596, A108

Planck Collaboration VI, 2020, A&A, 641, A6

Prevot M. L., Lequeux J., Maurice E., Prevot L., Rocca-Volmerange B., 1984, A&A, 132, 389

Prieto-Lyon G. et al., 2023, A&A, 672, A186

Reddy N. A. et al., 2018, ApJ, 853, 56

Rieke M. J. et al., 2023a, ApJS, 269, 16

Rieke M. J. et al., 2023b, PASP, 135, 028001
Rinaldi P. et al., 2023a, preprint (arXiv:2309.15671)
Rinaldi P. et al., 2023b, ApJ, 952, 143
Robertson B. E., 2022, ARA&A, 60, 121
Robertson B. E. et al., 2013, ApJ, 768, 71
Robertson B. E., Ellis R. S., Furlanetto S. R., Dunlop J. S., 2015, ApJ, 802, L19
Rosdahl J. et al., 2018, MNRAS, 479, 994
Saxena A. et al., 2023, preprint (arXiv:2306.04536)
Seeyave L. T. C. et al., 2023, MNRAS, 525, 2422
Shivaei I. et al., 2018, ApJ, 855, 42
Shivaei I. et al., 2020, ApJ, 899, 117
Simmonds C. et al., 2023, MNRAS, 523, 5468
Song M. et al., 2016, ApJ, 825, 5
Stark D. P., Schenker M. A., Ellis R., Robertson B., McLure R., Dunlop J., 2013, ApJ, 763, 129
Stark D. P. et al., 2015, MNRAS, 454, 1393
Stark D. P. et al., 2017, MNRAS, 464, 469
Stefanon M., Bouwens R. J., Illingworth G. D., Labbé I., Oesch P. A., Gonzalez V., 2022, ApJ, 935, 94
Steidel C. C., Bogosavljević M., Shapley A. E., Reddy N. A., Rudie G. C., Pettini M., Trainor R. F., Strom A. L., 2018, ApJ, 869, 123
Stinson G. S., Dalcanton J. J., Quinn T., Kaufmann T., Wadsley J., 2007, ApJ, 667, 170
Sugahara Y., Inoue A. K., Fudamoto Y., Hashimoto T., Harikane Y., Yamanaka S., 2022, ApJ, 935, 119
Sun G., Furlanetto S. R., 2016, MNRAS, 460, 417
Tacchella S., Forbes J. C., Caplar N., 2020, MNRAS, 497, 698
Tacchella S. et al., 2022a, MNRAS, 513, 2904
Tacchella S. et al., 2022b, ApJ, 927, 170
Tacchella S. et al., 2023, MNRAS, 522, 6236
Tang M., Stark D. P., Chevallard J., Charlot S., 2019, MNRAS, 489, 2572
Tang M. et al., 2023, MNRAS, 526, 1657
Trebitsch M., Volonteri M., Dubois Y., 2020, MNRAS, 494, 3453
Vanzella E. et al., 2018, MNRAS, 476, L15
Vijayan A. P., Lovell C. C., Wilkins S. M., Thomas P. A., Barnes D. J., Irodotou D., Kuusisto J., Roper W. J., 2021, MNRAS, 501, 3289
Virtanen P. et al., 2020, Nat. Methods, 17, 261
Weisz D. R. et al., 2012, ApJ, 744, 44
Williams C. C. et al., 2023, ApJS, 268, 64
Yang J. et al., 2020, ApJ, 904, 26
Yeh J. Y. C. et al., 2023, MNRAS, 520, 2757

SUPPORTING INFORMATION

Supplementary data are available at *MNRAS* online.

suppl_data

Please note: Oxford University Press is not responsible for the content or functionality of any supporting materials supplied by the authors. Any queries (other than missing material) should be directed to the corresponding author for the article.

APPENDIX A: PROSPECTOR RESULTS

Here, we present the galaxy properties inferred by PROSPECTOR. They are shown visually in Fig. A1, and as a table in Table A1.
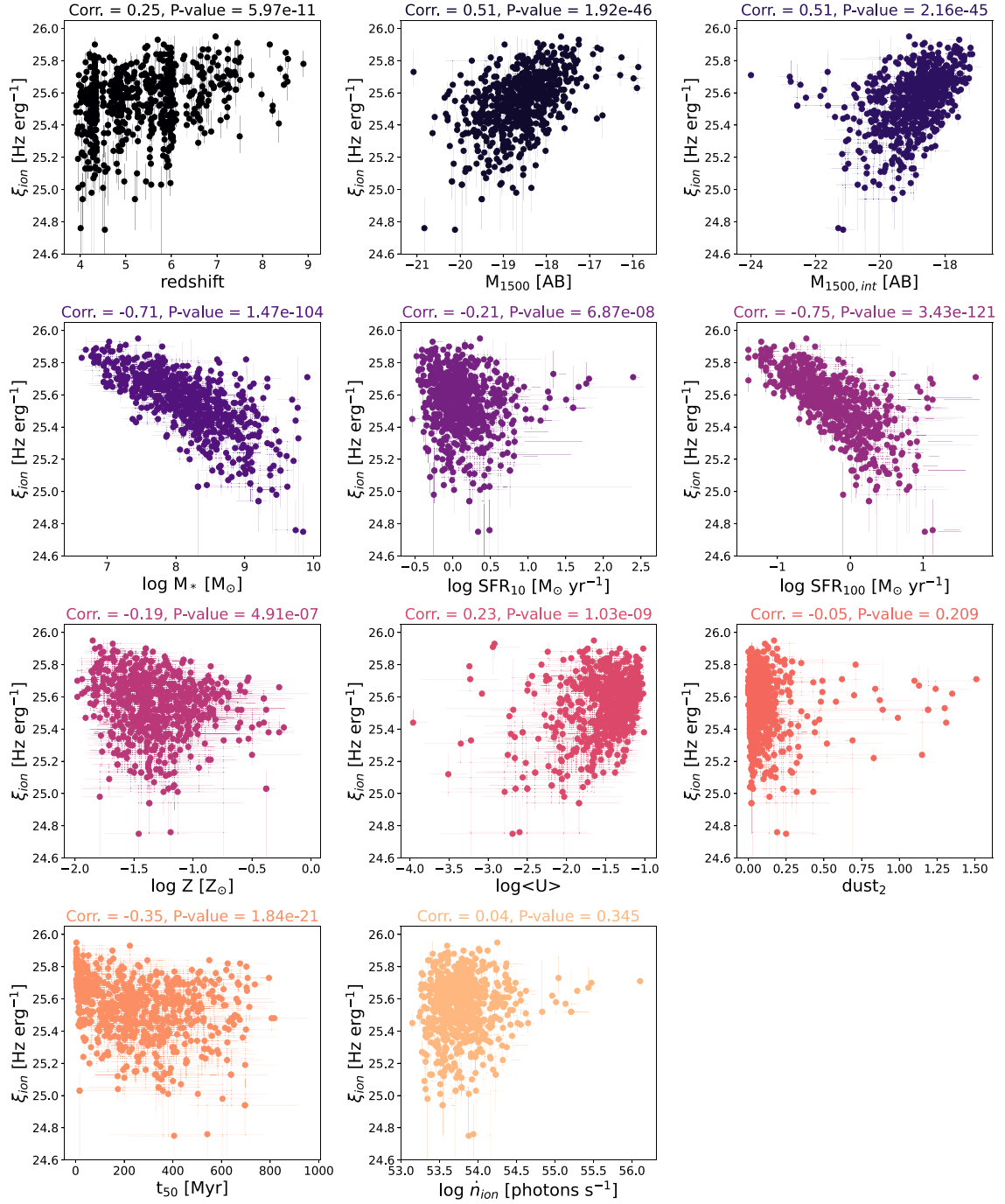
Figure A1. Exploring tentative correlations between $\xi_{\rm ion}$ and different properties. The vertical axis is $\xi_{\rm ion}$ in all panels, while the name of each property is given in the *x*-label. The title of the panels show the Spearman's rank coefficients for each parameter, indicating how strong the correlation is with $\xi_{\rm ion}$. The strongest correlations are found for SFR_{100} (right panel of second row) and stellar mass (left panel of second row). From top to bottom and left to right, the parameters are: redshift, observed UV magnitude (M_{1500}), intrinsic UV magnitude ($M_{1500,\,\rm int}$), stellar mass (M_*), SFR in the past 10 Myr (SFR_{10}), SFR in the past 100 Myr (SFR_{100}), metallicity (Z), ionization parameter ($\log\langle U\rangle$), dust2, half-mass assembly time (t50), and rate of ionizing photons being emitted ($\dot{n}_{\rm ion}$).

Table A1. Table excerpt showing a selection of galaxies in our sample, for clarity, we have chosen to display the results for the same galaxies shown in Table 1.

Name	z	M_{1500} [AB]	$M_{1500,int}$ [AB]	$\log M$ [$M_\odot$]	$\log SFR_{10}$ [$M_\odot$ yr^{-1}]	$\log SFR_{100}$ [$M_\odot$ yr^{-1}]	$\log Z$ [$Z_\odot$]	$\log(U)$	$dust_2$	t_{50} [Myr]	$\dot{n}_{ion}$ [s^{-1}]
JADES-GS + 53.11634−27.81272	3.91 ± 0.05	$-19.52^{0.05}_{-0.03}$	$-19.52^{0.06}_{-0.07}$	$8.98^{0.05}_{-0.19}$	$0.34^{0.06}_{-0.06}$	$0.09^{0.19}_{-0.11}$	$-1.14^{0.32}_{-0.22}$	$-1.34^{0.27}_{-0.33}$	$0.02^{0.03}_{-0.01}$	$817.19^{141.22}_{-381.59}$	$53.94^{0.02}_{-0.05}$
JADES-GS + 53.20925−27.75711	3.92 ± 0.04	$-17.51^{0.07}_{-0.07}$	$-17.69^{0.10}_{-0.19}$	$7.96^{0.15}_{-0.13}$	$-0.39^{0.11}_{-0.08}$	$-0.68^{0.18}_{-0.09}$	$-1.13^{0.31}_{-0.50}$	$-1.25^{0.15}_{-0.53}$	$0.05^{0.06}_{-0.03}$	$502.82^{116.09}_{-298.10}$	$53.25^{0.07}_{-0.04}$
JADES-GS + 53.12549−27.78044	3.94 ± 0.05	$-19.55^{0.04}_{-0.04}$	$-19.51^{0.05}_{-0.11}$	$8.44^{0.09}_{-0.06}$	$0.23^{0.10}_{-0.06}$	$0.13^{0.08}_{-0.04}$	$-1.59^{0.23}_{-0.14}$	$-1.66^{0.36}_{-0.26}$	$0.01^{0.03}_{-0.01}$	$302.96^{66.06}_{-177.69}$	$53.82^{0.04}_{-0.02}$
JADES-GS + 53.18436−27.80581	3.95 ± 0.04	$-19.15^{0.11}_{-0.09}$	$-20.51^{0.46}_{-0.66}$	$9.71^{0.08}_{-0.13}$	$0.50^{0.00}_{-0.18}$	$0.62^{0.05}_{-0.15}$	$-1.24^{0.47}_{-0.26}$	$-2.52^{1.01}_{-0.90}$	$0.32^{0.30}_{-0.15}$	$697.12^{132.32}_{-224.10}$	$54.06^{0.29}_{-0.15}$
JADES-GS + 53.16268−27.73611	3.95 ± 0.04	$-18.06^{0.06}_{-0.05}$	$-18.26^{0.16}_{-0.15}$	$8.71^{0.04}_{-0.15}$	$-0.39^{0.18}_{-0.09}$	$-0.40^{0.04}_{-0.14}$	$-1.69^{0.55}_{-0.21}$	$-1.43^{0.26}_{-0.42}$	$0.07^{0.05}_{-0.05}$	$560.40^{174.10}_{-171.13}$	$53.32^{0.05}_{-0.06}$
JADES-GS + 53.15123−27.79826	3.96 ± 0.04	$-18.35^{0.07}_{-0.07}$	$-19.63^{0.43}_{-0.53}$	$9.22^{0.14}_{-0.17}$	$0.02^{0.69}_{-0.14}$	$0.35^{0.69}_{-0.14}$	$-1.25^{0.36}_{-0.41}$	$-2.05^{0.60}_{-0.84}$	$0.32^{0.26}_{-0.17}$	$502.74^{290.13}_{-220.83}$	$53.51^{0.26}_{-0.13}$
JADES-GS + 53.15282−27.79549	3.97 ± 0.04	$-18.09^{0.00}_{-0.06}$	$-18.06^{0.10}_{-0.01}$	$7.59^{0.17}_{-0.13}$	$-0.11^{0.00}_{-0.04}$	$-0.92^{0.08}_{-0.00}$	$-1.03^{0.11}_{-0.04}$	$-1.20^{0.11}_{-0.02}$	$0.04^{0.01}_{-0.03}$	$557.16^{40.65}_{-51.46}$	$53.57^{0.05}_{-0.05}$
JADES-GS + 53.19804−27.76002	3.97 ± 0.04	$-18.48^{0.06}_{-0.05}$	$-18.69^{0.15}_{-0.19}$	$8.68^{0.12}_{-0.23}$	$-0.08^{1.22}_{-0.10}$	$-0.17^{0.30}_{-0.12}$	$-1.04^{0.53}_{-0.46}$	$-1.26^{0.21}_{-0.25}$	$0.05^{0.06}_{-0.03}$	$586.50^{49.05}_{-213.14}$	$53.53^{0.05}_{-0.05}$
JADES-GS + 53.13905−27.75893	3.97 ± 0.05	$-19.04^{0.06}_{-0.03}$	$-18.93^{0.09}_{-0.08}$	$8.01^{0.05}_{-0.08}$	$0.17^{0.06}_{-0.03}$	$-0.16^{0.09}_{-0.21}$	$-1.84^{0.61}_{-0.09}$	$-1.39^{0.22}_{-0.10}$	$0.02^{0.01}_{-0.01}$	$97.09^{337.60}_{-15.53}$	$53.88^{0.02}_{-0.03}$
JADES-GS + 53.15186−27.75258	4.00 ± 0.06	$-17.80^{0.04}_{-0.05}$	$-17.85^{0.15}_{-0.21}$	$7.43^{0.12}_{-0.16}$	$-0.31^{0.09}_{-0.04}$	$-0.66^{0.17}_{-0.10}$	$-1.22^{0.17}_{-0.16}$	$-1.23^{0.12}_{-0.16}$	$0.03^{0.04}_{-0.02}$	$41.59^{79.71}_{-24.23}$	$53.39^{0.05}_{-0.03}$
JADES-GS + 53.12644−27.79200	5.37 ± 0.06	$-18.49^{0.03}_{-0.03}$	$-18.35^{0.06}_{-0.17}$	$7.37^{0.21}_{-0.09}$	$-0.00^{0.05}_{-0.03}$	$-0.77^{0.15}_{-0.09}$	$-1.61^{0.61}_{-0.29}$	$-1.10^{0.08}_{-0.20}$	$0.01^{0.03}_{-0.01}$	$43.43^{183.82}_{-33.08}$	$53.78^{0.03}_{-0.03}$
JADES-GS + 53.12775−27.78098	5.38 ± 0.06	$-18.48^{0.06}_{-0.03}$	$-19.03^{0.20}_{-0.14}$	$8.29^{0.24}_{-0.48}$	$0.17^{0.22}_{-0.09}$	$-0.22^{0.74}_{-0.11}$	$-1.12^{0.50}_{-0.58}$	$-1.26^{0.19}_{-0.26}$	$0.10^{0.07}_{-0.05}$	$320.79^{173.58}_{-300.27}$	$53.79^{0.05}_{-0.07}$
JADES-GS + 53.16729−27.75273	5.38 ± 0.06	$-18.88^{0.03}_{-0.03}$	$-18.91^{0.09}_{-0.15}$	$8.48^{0.13}_{-0.16}$	$-0.02^{0.15}_{-0.06}$	$-0.00^{0.31}_{-0.11}$	$-1.33^{0.31}_{-0.33}$	$-1.36^{0.23}_{-0.37}$	$0.03^{0.05}_{-0.02}$	$303.50^{119.74}_{-151.42}$	$53.66^{0.08}_{-0.05}$
JADES-GS + 53.14381−27.80835	5.42 ± 0.08	$-17.93^{0.03}_{-0.03}$	$-17.80^{0.06}_{-0.08}$	$7.24^{0.16}_{-0.53}$	$-0.21^{0.05}_{-0.09}$	$-0.92^{0.78}_{-0.12}$	$-1.46^{0.19}_{-0.31}$	$-1.30^{0.16}_{-0.32}$	$0.01^{0.01}_{-0.01}$	$25.68^{86.95}_{-19.30}$	$53.49^{0.03}_{-0.03}$
JADES-GS + 53.10726−27.81102	5.43 ± 0.07	$-16.82^{0.15}_{-0.12}$	$-17.21^{0.14}_{-0.06}$	$6.69^{0.53}_{-0.14}$	$-0.41^{0.05}_{-0.05}$	$-1.40^{0.30}_{-0.10}$	$-1.76^{0.09}_{-0.16}$	$-1.83^{0.30}_{-0.50}$	$0.10^{0.05}_{-0.03}$	$4.34^{247.58}_{-1.81}$	$53.41^{0.06}_{-0.02}$
JADES-GS + 53.14676−27.79738	5.43 ± 0.06	$-17.92^{0.03}_{-0.04}$	$-17.81^{0.07}_{-0.13}$	$7.30^{0.12}_{-0.21}$	$-0.23^{0.02}_{-0.04}$	$-0.92^{0.23}_{-0.07}$	$-1.27^{0.15}_{-0.51}$	$-1.70^{0.52}_{-0.38}$	$0.01^{0.03}_{-0.01}$	$42.70^{234.59}_{-28.41}$	$53.48^{0.03}_{-0.02}$
JADES-GS + 53.12301−27.79661	5.44 ± 0.06	$-18.04^{0.04}_{-0.04}$	$-18.22^{0.06}_{-0.05}$	$7.11^{0.07}_{-0.06}$	$-0.04^{0.03}_{-0.02}$	$-0.92^{0.04}_{-0.07}$	$-1.25^{0.08}_{-0.08}$	$-1.45^{0.32}_{-0.15}$	$0.04^{0.04}_{-0.01}$	$4.92^{3.41}_{-0.92}$	$53.74^{0.02}_{-0.02}$
JADES-GS + 53.12247−27.79653	5.44 ± 0.07	$-18.11^{0.04}_{-0.03}$	$-18.52^{0.06}_{-0.27}$	$7.75^{0.17}_{-0.17}$	$0.06^{0.08}_{-0.05}$	$-0.59^{0.00}_{-0.18}$	$-1.51^{0.59}_{-0.05}$	$-1.67^{0.23}_{-0.61}$	$0.09^{0.07}_{-0.02}$	$31.12^{423.39}_{-27.09}$	$53.75^{0.05}_{-0.04}$
JADES-GS + 53.16407−27.79972	5.44 ± 0.08	$-20.19^{0.03}_{-0.03}$	$-20.21^{0.06}_{-0.13}$	$9.08^{0.13}_{-0.29}$	$0.27^{0.32}_{-0.13}$	$0.67^{0.18}_{-0.11}$	$-1.16^{0.33}_{-0.35}$	$-2.19^{0.45}_{-0.79}$	$0.02^{0.05}_{-0.01}$	$341.47^{174.28}_{-286.55}$	$53.79^{0.10}_{-0.08}$
JADES-GS + 53.12874−27.79788	5.44 ± 0.06	$-17.92^{0.03}_{-0.04}$	$-18.10^{0.12}_{-0.25}$	$7.95^{0.11}_{-0.28}$	$-0.12^{0.08}_{-0.07}$	$-0.64^{0.22}_{-0.12}$	$-1.28^{0.49}_{-0.38}$	$-1.36^{0.29}_{-0.23}$	$0.06^{0.06}_{-0.03}$	$376.88^{131.65}_{-299.49}$	$53.56^{0.07}_{-0.06}$
JADES-GS + 53.19106−27.79732	7.26 ± 0.07	$-19.13^{0.04}_{-0.04}$	$-19.96^{0.31}_{-0.32}$	$8.51^{0.15}_{-0.30}$	$0.54^{0.14}_{-0.08}$	$0.19^{0.91}_{-0.16}$	$-1.62^{0.43}_{-0.20}$	$-1.85^{0.33}_{-0.36}$	$0.18^{0.11}_{-0.09}$	$103.35^{157.81}_{-74.78}$	$54.20^{0.13}_{-0.10}$
JADES-GS + 53.17976−27.77465	7.27 ± 0.08	$-19.15^{0.05}_{-0.03}$	$-20.70^{0.60}_{-0.32}$	$8.66^{0.10}_{-0.15}$	$0.87^{0.13}_{-0.16}$	$0.47^{0.51}_{-0.12}$	$-1.55^{0.28}_{-0.22}$	$-1.67^{0.51}_{-0.14}$	$0.49^{0.26}_{-0.28}$	$90.19^{102.14}_{-43.73}$	$54.55^{0.22}_{-0.15}$
JADES-GS + 53.16579−27.82179	7.29 ± 0.09	$-17.91^{0.04}_{-0.04}$	$-18.41^{0.15}_{-0.26}$	$7.43^{0.35}_{-0.36}$	$0.04^{0.06}_{-0.06}$	$-0.72^{0.28}_{-0.17}$	$-1.48^{0.43}_{-0.42}$	$-1.67^{0.33}_{-0.70}$	$0.10^{0.09}_{-0.03}$	$53.84^{241.98}_{-50.66}$	$53.79^{0.05}_{-0.07}$
JADES-GS + 53.18334−27.79050	7.30 ± 0.07	$-17.82^{0.09}_{-0.10}$	$-18.76^{0.18}_{-0.28}$	$7.73^{0.22}_{-0.28}$	$0.15^{0.19}_{-0.08}$	$-0.49^{0.30}_{-0.13}$	$-1.59^{0.54}_{-0.26}$	$-1.95^{0.60}_{-0.36}$	$0.15^{0.13}_{-0.06}$	$89.85^{92.18}_{-73.40}$	$53.89^{0.11}_{-0.08}$
JADES-GS + 53.13219−27.78578	7.39 ± 0.09	$-18.07^{0.05}_{-0.05}$	$-18.25^{0.16}_{-0.33}$	$7.42^{0.26}_{-0.21}$	$-0.05^{0.46}_{-0.04}$	$-0.74^{0.30}_{-0.12}$	$-1.52^{0.27}_{-0.32}$	$-1.32^{0.22}_{-0.34}$	$0.07^{0.20}_{-0.03}$	$87.39^{91.48}_{-79.55}$	$53.75^{0.06}_{-0.10}$
JADES-GS + 53.16638−27.81237	7.40 ± 0.08	$-17.78^{0.03}_{-0.06}$	$-17.73^{0.07}_{-0.10}$	$6.88^{0.34}_{-0.05}$	$-0.18^{0.02}_{-0.04}$	$-1.10^{0.60}_{-0.05}$	$-1.78^{0.21}_{-0.16}$	$-1.55^{0.30}_{-0.30}$	$0.04^{0.02}_{-0.02}$	$5.32^{18.39}_{-0.67}$	$53.53^{0.02}_{-0.03}$
JADES-GS + 53.18405−27.79783	7.41 ± 0.08	$-18.15^{0.09}_{-0.04}$	$-18.34^{0.16}_{-0.34}$	$7.25^{0.23}_{-0.26}$	$0.02^{0.06}_{-0.08}$	$-0.85^{0.00}_{-0.11}$	$-1.39^{0.51}_{-0.12}$	$-1.49^{0.36}_{-0.32}$	$0.07^{0.15}_{-0.02}$	$8.38^{49.78}_{-5.31}$	$53.71^{0.09}_{-0.03}$
JADES-GS + 53.18536−27.77319	7.41 ± 0.06	$-18.84^{0.03}_{-0.04}$	$-18.69^{0.23}_{-0.16}$	$7.41^{0.39}_{-0.35}$	$0.06^{0.14}_{-0.07}$	$-0.59^{0.00}_{-0.19}$	$-1.60^{0.45}_{-0.24}$	$-1.55^{0.35}_{-0.47}$	$0.01^{0.01}_{-0.00}$	$8.97^{32.63}_{-6.42}$	$53.77^{0.16}_{-0.09}$
JADES-GS + 53.18393−27.79999	7.42 ± 0.07	$-19.32^{0.04}_{-0.04}$	$-19.35^{0.11}_{-0.11}$	$8.19^{0.23}_{-0.48}$	$0.33^{0.09}_{-0.08}$	$-0.19^{0.31}_{-0.09}$	$-1.46^{0.34}_{-0.28}$	$-2.41^{0.86}_{-0.24}$	$0.02^{0.02}_{-0.01}$	$114.51^{185.35}_{-102.80}$	$54.00^{0.04}_{-0.07}$
JADES-GS + 53.18301−27.78946	7.45 ± 0.07	$-18.21^{0.04}_{-0.05}$	$-18.63^{0.09}_{-0.23}$	$7.27^{0.47}_{-0.12}$	$0.16^{0.04}_{-0.04}$	$-0.80^{1.20}_{-0.05}$	$-1.79^{0.13}_{-0.10}$	$-2.94^{0.35}_{-1.33}$	$0.13^{0.03}_{-0.02}$	$3.94^{132.92}_{-1.33}$	$54.01^{0.03}_{-0.06}$

Notes. Column 1: JADES identifier, composed of the coordinates of the centroid rounded to the fifth decimal place, in units of degrees. Column 2: photometric redshift inferred using the template-fitting code EAZY. Columns 3 and 4: observed and intrinsic UV magnitudes at rest-frame 1500 Å. Column 5: logarithm of the stellar mass in units of solar masses ($M_\odot$). Column 6: logarithm of the recent SFR (last 10 Myr) in units of $M_\odot$ yr^{-1}. Column 7: logarithm of the SFR in the past 100 Myr in units of $M_\odot$ yr^{-1}. Column 8: logarithm of the stellar metallicity in units of solar metallicities ($Z_\odot$). Column 9: dimensionless ionization parameter, $\log(U)$. Column 10: one of the governing dust parameters in the dust model adopted (see Conroy et al. 2009). Column 11: lookback time at which half of the mass was assembled in units of Myr. Column 12: ionizing photons emitted per second.

APPENDIX B: TRENDS WITH IONIZING PHOTON PRODUCTION

Fig. B1 shows the evolution of $\dot{n}_{\rm ion}$ as a function of $M_{\rm UV}$ for different redshift bins. $\dot{n}_{\rm ion}$ correlates negatively with UV magnitude, with a large scatter, indicating fainter galaxies produce in average a smaller amount of ionizing photons.
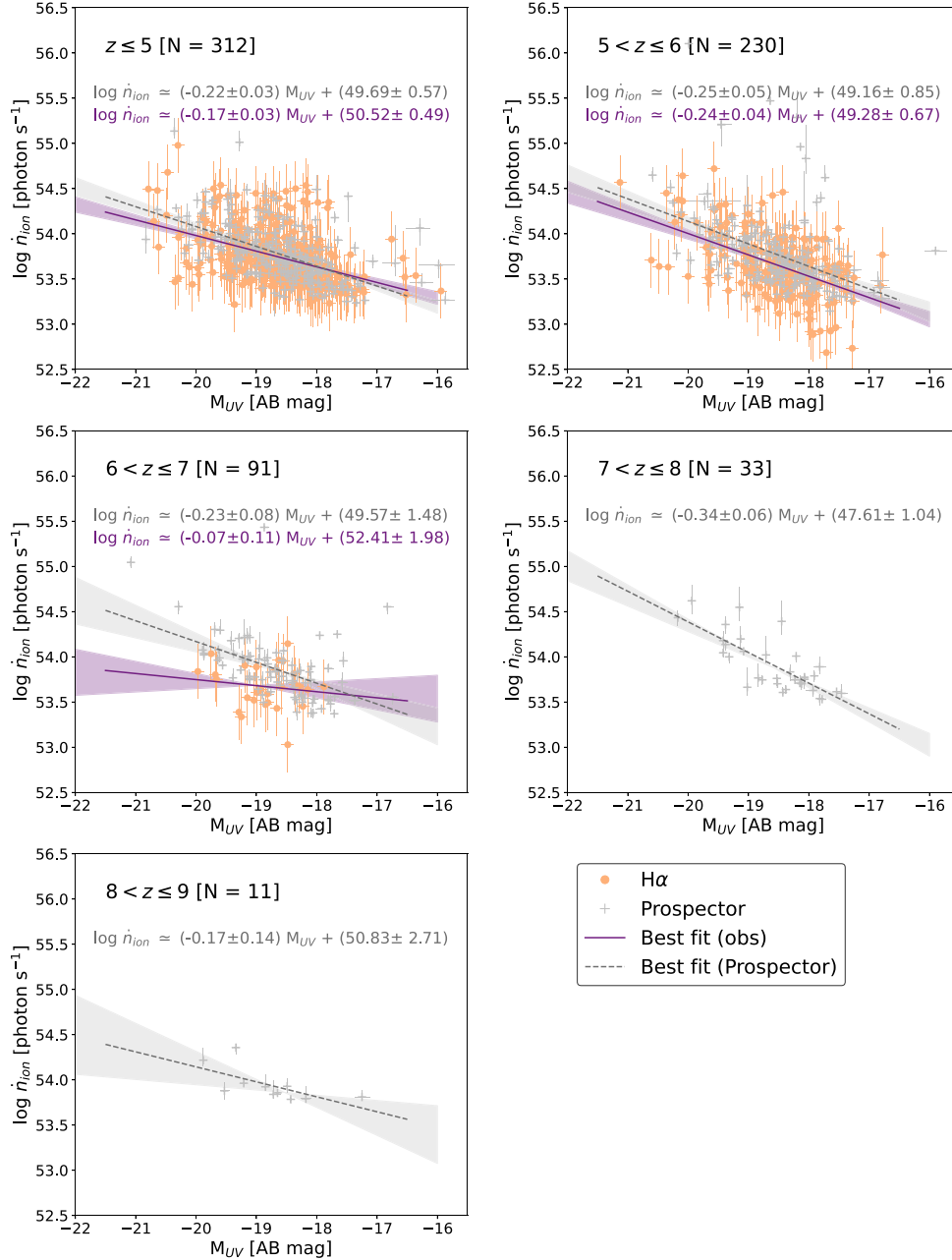
Figure B1. Evolution of $\dot{n}_{\rm ion}$ with UV magnitude, separated in redshift bins, analogous to Fig. 8. The coloured circles are values estimated from the dust-corrected Hα luminosities, as: $\dot{n}_{\rm ion} = 7.35 \times 10^{11}$ L(Hα). The number of galaxies in each redshift bin is indicated in the top left corner of each panel. The filled (dashed) line is the best fit to the data obtained via photometry (PROSPECTOR). Contrary to $\xi_{\rm ion}$, $\dot{n}_{\rm ion}$ decreases as galaxies become fainter.

This paper has been typeset from a TEX/LATEX file prepared by the author.